INVESTIGATING THE COSMIC-RAY IONIZATION RATE IN THE GALACTIC DIFFUSE INTERSTELLAR MEDIUM THROUGH OBSERVATIONS OF H_3^+

Nick Indriolo[1,3] and Benjamin J. McCall[1,2]
[1] Department of Astronomy, University of Illinois at Urbana-Champaign, Urbana, IL 61801, USA; indriolo@pha.jhu.edu
[2] Department of Chemistry, University of Illinois at Urbana-Champaign, Urbana, IL 61801, USA

ABSTRACT

Observations of H_3^+ in the Galactic diffuse interstellar medium have led to various surprising results, including the conclusion that the cosmic-ray ionization rate (ζ_2) is about one order of magnitude larger than previously thought. The present survey expands the sample of diffuse cloud sight lines with H_3^+ observations to 50, with detections in 21 of those. Ionization rates inferred from these observations are in the range $(1.7 \pm 1.3) \times 10^{-16}$ s^{-1} < ζ_2 < $(10.6 \pm 8.2) \times 10^{-16}$ s^{-1} with a mean value of $\zeta_2 = (3.5^{+5.3}_{-3.0}) \times 10^{-16}$ s^{-1}. Upper limits (3σ) derived from non-detections of H_3^+ are as low as $\zeta_2 < 0.4 \times 10^{-16}$ s^{-1}. These low upper limits, in combination with the wide range of inferred cosmic-ray ionization rates, indicate variations in ζ_2 between different diffuse cloud sight lines. A study of ζ_2 versus N_H (total hydrogen column density) shows that the two parameters are not correlated for diffuse molecular cloud sight lines, but that the ionization rate decreases when N_H increases to values typical of dense molecular clouds. Both the difference in ionization rates between diffuse and dense clouds and the variation of ζ_2 among diffuse cloud sight lines are likely the result of particle propagation effects. The lower ionization rate in dense clouds is due to the inability of low-energy (few MeV) protons to penetrate such regions, while the ionization rate in diffuse clouds is controlled by the proximity of the observed cloud to a site of particle acceleration.

Key words: cosmic rays

1. INTRODUCTION

The rich chemistry responsible for producing many of the small molecular species observed in the interstellar medium (ISM) is thought to be driven primarily by ion–molecule reactions (Watson 1973; Herbst & Klemperer 1973). To initiate this reaction network, a source of ionization is required that operates in both diffuse molecular ($n \sim 100$ cm^{-3}, $T \sim 70$ K) and dense molecular ($n \sim 10^4$ cm^{-3}, $T \sim 30$ K) clouds. As absorption by atomic hydrogen severely attenuates the flux of photons capable of ionizing many of the most abundant species in the molecular ISM (e.g., H_2, He, O), cosmic rays are the dominant ionization mechanism in such regions. This makes the cosmic-ray ionization rate a vital parameter in modeling interstellar chemistry.

Several estimates of the cosmic-ray ionization rate have been made over the past 50 years. Both theoretical calculations (e.g., Hayakawa et al. 1961; Spitzer & Tomasko 1968; Webber 1998) and observational inferences (e.g., O'Donnell & Watson 1974; Black & Dalgarno 1977; Black et al. 1978; Hartquist et al. 1978a, 1978b; van Dishoeck & Black 1986; Federman et al. 1996; van der Tak & van Dishoeck 2000; McCall et al. 2003; Indriolo et al. 2007; Gerin et al. 2010; Neufeld et al. 2010) produced a wide range of ionization rates, from a few times 10^{-18} s^{-1} to a few times 10^{-15} s^{-1}. However, many of the more recent values inferred for diffuse clouds have tended to be on the order of 10^{-16} s^{-1}.

Following its initial detection in the ISM (Geballe & Oka 1996), H_3^+ has widely been regarded as the most direct tracer of the cosmic-ray ionization rate (Dalgarno 2006) due to a simple underlying chemistry. Observations of H_3^+ in dense clouds (McCall et al. 1999; Kulesa 2002; Brittain et al. 2004; Gibb et al. 2010), diffuse clouds (McCall et al. 1998, 2002, 2003; Indriolo

et al. 2007, 2010; Crabtree et al. 2011), and toward the Galactic center (Geballe et al. 1999; Goto et al. 2002, 2008, 2011; Oka et al. 2005; Geballe & Oka 2010) can be and have been used to constrain the ionization rate in each of these environments. Here we present the most comprehensive survey of H_3^+ in diffuse molecular cloud sight lines to date, expanding and improving upon our analysis from Indriolo et al. (2007).

2. H_3^+ CHEMISTRY

As mentioned above, the chemistry associated with H_3^+ in the ISM is rather simple. H_3^+ is formed in a two-step process, beginning with the ionization of H_2 by cosmic rays,
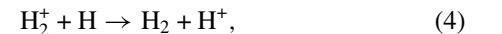
$$H_2 + CR \rightarrow H_2^+ + e^- + CR', \tag{1}$$
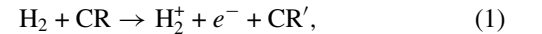
and quickly followed by a reaction of H_2^+ with H_2,

$$H_2^+ + H_2 \rightarrow H_3^+ + H. \tag{2}$$
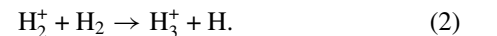
Some amount of H_2^+ will be destroyed by dissociative recombination with electrons,

$$H_2^+ + e^- \rightarrow H + H, \tag{3}$$

or charge transfer to atomic hydrogen,

$$H_2^+ + H \rightarrow H_2 + H^+, \tag{4}$$

before it can form H_3^+, but these processes are slow compared to reaction (2). Overall, reaction (1) is the rate-limiting step (it is many orders of magnitude slower than reaction (2)) and can be taken as the formation rate of H_3^+. Photoionization of H_2 also occurs, but is negligible compared to ionization by cosmic rays. This is because the ultraviolet and soft X-ray photons capable of ionizing H_2 ($E > 15.4$ eV) are severely attenuated in the outer layers of diffuse clouds by atomic hydrogen, which has a lower
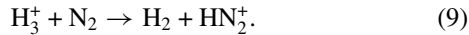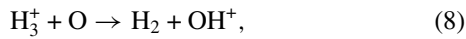
ionization potential (13.6 eV). While higher energy photons (e.g., hard X-rays and γ-rays) can penetrate diffuse molecular clouds, the lower ionization cross sections at these energies and smaller flux of such photons make their contribution to the ionization rate minimal. As a result, H_3^+ should be formed primarily through the ionization of H_2 by cosmic rays.

The primary destruction mechanisms for H_3^+ are dependent on the environment under consideration. In diffuse molecular clouds, H_3^+ is predominantly destroyed via dissociative recombination with electrons,

$$H_3^+ + e^- \rightarrow H_2 + H \text{ or } H + H + H. \tag{5}$$
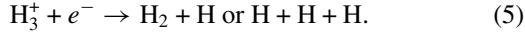
In dense clouds however, where the electron fraction is much lower, H_3^+ is destroyed by proton transfer to neutrals such as CO, O, and N_2:

$$H_3^+ + CO \rightarrow H_2 + HCO^+, \tag{6}$$

$$H_3^+ + CO \rightarrow H_2 + HOC^+, \tag{7}$$

$$H_3^+ + O \rightarrow H_2 + OH^+, \tag{8}$$

$$H_3^+ + N_2 \rightarrow H_2 + HN_2^+. \tag{9}$$

These ion–molecule reactions demonstrate how H_3^+ essentially drives the chemistry in the ISM by generating molecular ions which can then go on to form even more complex species. Because the chemistry surrounding H_3^+ is so simple, and because its formation arises directly as a result of ionization by cosmic rays, observations of H_3^+ can be a powerful probe of the cosmic-ray ionization rate.

3. METHODS

3.1. Observations

In diffuse molecular clouds, conditions are such that only the two lowest energy levels of H_3^+—the $(J, K) = (1, 1)$ *para* and $(1, 0)$ *ortho* states—are expected to be significantly populated. As a result, observations that probe transitions arising from these two states will trace the entire content of H_3^+ along a line of sight. We targeted three such transitions—the $R(1, 1)^u$, $R(1, 0)$, and $R(1, 1)^l$—which are observable at 3.668083 μm, 3.668516 μm, and 3.715479 μm, respectively. As the weak H_3^+ lines are located near various atmospheric CH_4 and HDO lines, precise removal of the telluric lines is vital for the purpose of accurately determining H_3^+ column densities, and is facilitated by the observation of telluric standard stars. Because the $R(1, 1)^u$ and $R(1, 0)$ transitions are easily observed simultaneously (being separated by about 4 Å), and because together they probe the entire population of H_3^+, they are the most frequently observed transitions.

Although observations of H_3^+ have become more common-place, as evidenced by the publication list in Section 1, they are still rather difficult. Given the transition dipole moments (see, e.g., Goto et al. 2002, and references therein) and a typical relative abundance of about 10^{-7} to 10^{-8} with respect to H_2, H_3^+ absorption lines in diffuse molecular clouds are usually about 1%–2% deep, and thus require a signal-to-noise ratio (S/N) greater than about 300 on the continuum to achieve 3σ detections. As a result, background sources must have L-band (3.5 μm) magnitudes brighter than about $L = 7.5$ mag to be feasible targets for 8 m (or $L = 5.5$ mag for 4 m) class

telescopes. Ideally, these background sources should also be early-type stars (OB) such that the continuum is free of stellar absorption features. A list of all background sources targeted in our study, along with select line-of-sight properties, is presented in Table 1. Additionally, to adequately sample the intrinsically narrow interstellar absorption lines requires high spectroscopic resolving power ($R \gtrsim 20{,}000$).

Observations used in this study were taken between 1998 and 2010 with a variety of instrument/telescope combinations, including CGS4 (Mountain et al. 1990) at UKIRT, NIRSPEC (McLean et al. 1998) at Keck, Phoenix (Hinkle et al. 2003) at both KPNO and Gemini South, and CRIRES (Käufl et al. 2004) at the Very Large Telescope (VLT). A log of all H_3^+ observations in diffuse molecular clouds utilized herein—including those previously published—can be found in Table 2.4 of Indriolo (2011). For specifics regarding instrument configurations, observing methods and the like, the reader is referred to the following sources: McCall et al. (1998, 2002, 2003); McCall (2001); Geballe et al. (1999); Indriolo et al. (2007, 2010); Indriolo (2011); Crabtree et al. (2011).

3.2. Data Reduction

Beginning with raw data frames, our reduction procedure employed standard IRAF[4] routines commonly used in spectroscopic data reduction. Upon extracting one-dimensional spectra, data were transferred to Igor Pro[5] where we have macros written to complete the reduction (McCall 2001). Spectra published in Indriolo et al. (2007) were reprocessed here using a method that better accounts for bad pixels in the CGS4 array. A full description of the new reduction procedure used for CGS4 data—and all of our reduction procedures applying to H_3^+ data in general—is presented in Indriolo (2011).

4. UPDATED RESULTS

Fully reduced spectra are presented in Figures 1–13. Of the 42 sight lines presented, 15 show H_3^+ absorption lines, while 27 do not. Combining these results with the spectra presented in McCall et al. (2002), our entire survey covers 50 diffuse molecular cloud sight lines, with H_3^+ detections in 21 of those.

As mentioned above, all of the spectra presented in Indriolo et al. (2007) were reprocessed for this study. In most cases the differences between the resulting spectra are minimal, but spectra presented herein, along with any results derived from them, should be regarded as superseding any previously published results. There are four sight lines in particular where further discussion of new versus old spectra is warranted: BD $-14\ 5037$, HD 154368, ζ Per, and X Per. In Indriolo et al. (2007) we reported a detection of H_3^+ toward BD $-14\ 5037$—albeit marginal at best—but with the updated reduction procedure this sight line is now considered to be a non-detection (see Figure 6 herein versus Figure 3 from Indriolo et al. 2007). Spectra toward HD 154368, ζ Per, and X Per were reported in Crabtree et al. (2011), but we later realized that an important step in the reduction process was omitted for these three sight lines; spectra taken at the A and B nod positions had been combined based solely on pixel number without accounting for any potential shift in the dispersion direction. For both HD 154368 and ζ Per the effects of reprocessing the data were minimal, and newly derived column densities and *para* fractions agree with those reported in Crabtree et al. (2011) within uncertainties. For X Per though,

---

4 http://iraf.noao.edu/
5 http://www.wavemetrics.com/

Table 1
Science Targets

Object	HD Number	$E(B-V)$ (mag)	Ref.	Distance (pc)	Ref.
κ Cas	2905	0.33	1	1370	11
HD 20041	20041	0.72	2	1400	2
HD 21483	21483	0.56	2	440	2
HD 21389	21389	0.57	2	940	2
HD 21856	21856	0.19	3	502	11
40 Per	22951	0.27	1	283	11
o Per	23180	0.31	2	280	2
BD +31 643	281159	0.85	2	240	2
ζ Per	24398	0.31	2	301	2
X Per	24534	0.59	2	590	2
ϵ Per	24760	0.09	3	196	11
ξ Per	24912	0.33	2	470	2
62 Tau	27778	0.37	2	223	2
HD 29647	29647	1.00	2	177	2
α Cam	30614	0.30	2	820	2
NGC 2024 IRS 1	...	1.69	4	450	4
χ^2 Ori	41117	0.45	2	1000	2
HD 47129	47129	0.36	1	1514	12
HD 53367	53367	0.74	2	780	2
HD 73882	73882	0.70	5	1000	13
HD 110432	110432	0.51	5	300	14
o Sco	147084	0.74	4	270	11
ρ Oph D	147888	0.47	2	136	2
HD 147889	147889	1.07	2	136	2
χ Oph	148184	0.52	1	161	5
μ Nor	149038	0.38	3	1122	12
HD 149404	149404	0.68	1	417	11
ζ Oph	149757	0.32	2	140	2
HD 152236	152236	0.68	5	600	15
HD 154368	154368	0.78	5	909	16
WR 104	...	2.30	6	2600	17
HD 168607	168607	1.61	7	1100	7
HD 168625	168625	1.86	8	2800	18
BD -14 5037	...	1.57	4	1700	4
HD 169454	169454	1.12	2	930	2
W40 IRS 1A	...	2.90	9	400	9
WR 118	...	4.57	6	3900	6
WR 121	...	1.75	6	2600	6
HD 183143	183143	1.28	7	1000	7
P Cygni	193237	0.63	7	1800	7
HD 193322A	193322A	0.40	3	830	19
HD 229059	229059	1.71	2	1000	2
HD 194279	194279	1.22	7	1100	7
Cyg OB2 5	...	1.99	7	1700	7
Cyg OB2 12	...	3.35	7	1700	7
Cyg OB2 8A	...	1.60	10	1700	7
HD 204827	204827	1.11	2	600	2
HD 206267	206267	0.53	2	1000	2
19 Cep	209975	0.36	1	1300	20
λ Cep	210839	0.57	2	505	2
1 Cas	218376	0.25	2	339	2

Notes.

References. (1) McCall et al. 2010; (2) Thorburn et al. 2003; (3) Savage et al. 1977; (4) van Dishoeck & Black 1989; (5) Rachford et al. 2009; (6) Conti & Vacca 1990; (7) McCall et al. 2002, and references therein; (8) Nota et al. 1996; (9) Shuping et al. 1999; (10) Snow et al. 2010; (11) van Leeuwen 2007; (12) Fruscione et al. 1994; (13) Nichols & Slavin 2004; (14) Chevalier & Ilovaisky 1998; (15) Ritchey et al. 2011; (16) Maíz-Apellániz et al. 2004; (17) Tuthill et al. 2008; (18) Pasquali et al. 2002; (19) Roberts et al. 2010; (20) Sheffer et al. 2008.

individual spectra had relatively low S/N and a large number of frames were shifted in the dispersion direction, thus the new reduction is significantly different from that reported in Crabtree et al. (2011). By using the new X Per results (see Table 2) in the analysis presented by Crabtree et al. (2011), the conclusions in that study are actually strengthened, as the erroneous X Per data used therein consistently made that sight line the only outlier in the reported trends.

5. ANALYSIS

5.1. Extraction of Column Densities and Upper Limits

Absorption features due to H_3^+ were fit with Gaussian functions in order to determine equivalent widths, velocity FWHM, and interstellar gas velocities. The fitting procedure uses the functional form of a Gaussian where the area (as opposed to amplitude) is a free parameter, and includes a fit to the continuum level; i.e.,

$$I = I_0 - \frac{A}{w\sqrt{\pi}} \exp\left[-\left(\frac{\lambda - \lambda_0}{w}\right)^2\right], \qquad (10)$$

and was developed in Igor Pro. The free parameters here are the continuum level, I_0, the area of the Gaussian, A, the central wavelength of the Gaussian, λ_0, and the line width, w (note that the width used here is related to the "standard" Gaussian width, σ, by $w^2 = 2\sigma^2$). As the continuum level has already been normalized, an area determined using this fit is by definition an equivalent width, W_λ. In the case of the $R(1,1)^u$ and $R(1,0)$ lines, both absorption features are fit simultaneously and a single best-fit continuum level is found. Uncertainties on the equivalent widths (δW_λ) and continuum level (δI)—both at the 1σ level—are found by the fitting process. To estimate the systematic uncertainties due to continuum placement, the continuum level was forced to $I_0 + \delta I$ and $I_0 - \delta I$ and the absorption lines re-fit. Variations in the equivalent widths due to this shift are small compared to those reported by the fitting procedure and so have been ignored (i.e., $\sigma(W_\lambda) = \delta W_\lambda$). Assuming optically thin absorption lines and taking transition dipole moments and wavelengths from Goto et al. (2002, and references therein), column densities are derived from equivalent widths using the standard relation:

$$N(J, K) = \left(\frac{3hc}{8\pi^3}\right) \frac{W_\lambda}{\lambda} \frac{1}{|\mu|^2}, \qquad (11)$$

where $N(J,K)$ is the column density in the state from which the transition arises, h is Planck's constant, c is the speed of light, λ is the transition wavelength, and $|\mu|^2$ is the square of the transition dipole moment.

In cases where H_3^+ absorption lines are not detected, upper limits to the equivalent width are computed as

$$W_\lambda < \sigma \lambda_{\text{pix}} \sqrt{\mathcal{N}_{\text{pix}}}, \qquad (12)$$

where σ is the standard deviation on the continuum level near the expected H_3^+ lines, λ_{pix} is the wavelength coverage per pixel, and $\mathcal{N}_{\text{pix}}$ is the number of pixels expected in an absorption feature. Upper limits to the column density are then determined
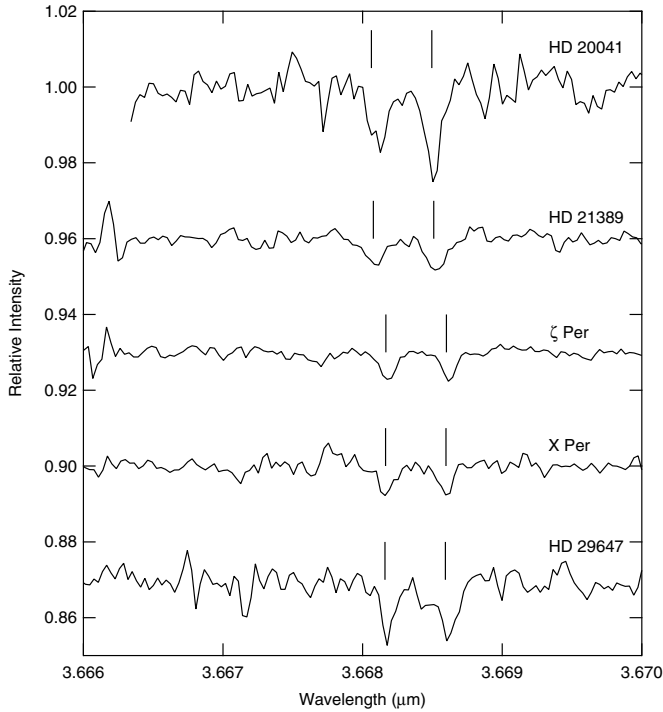
Figure 1. Spectra targeting the $R(1, 1)^u$ and $R(1, 0)$ lines of H_3^+ in the sight lines toward HD 20041, HD 21389, ζ Per, X Per, and HD 29647. Vertical lines mark the expected positions of absorption lines given gas velocities along each line of sight. Gaps in spectra are where the removal of atmospheric features was particularly poor. Observations were made with CGS4 at UKIRT.
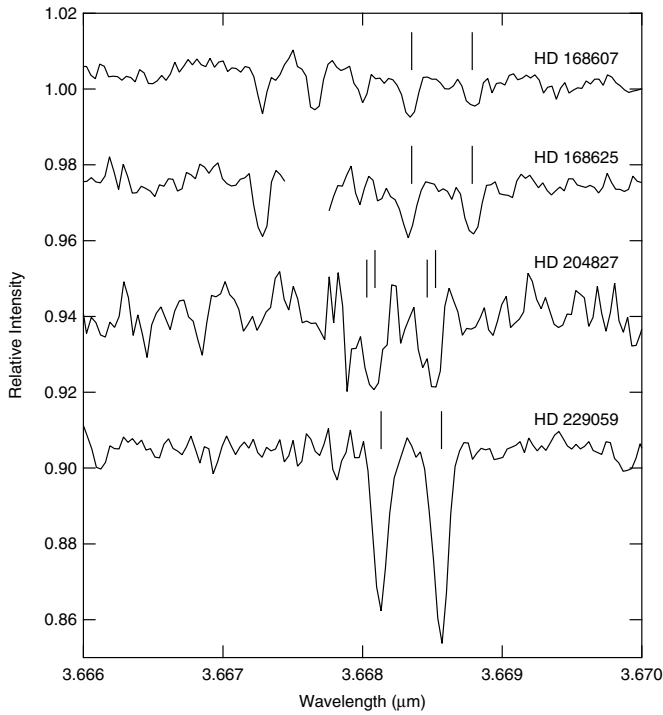

Figure 3. Same as Figure 1 except for the sight lines toward HD 169454 and W40 IRS 1A.

Figure 2. Same as Figure 1 except for the sight lines toward HD 168607, HD 168625, HD 204827, and HD 229059.

Figure 4. Same as Figure 3 except targeting the $R(1, 1)^l$ transition.

5.2. Determination of the Cosmic-ray Ionization Rate

As discussed in Section 2, the chemistry associated with H_3^+ in diffuse molecular clouds is rather simple. Assuming steady-state conditions, the formation and destruction rates of H_3^+ can be equated. In the simplified version of diffuse cloud chemistry—where destruction occurs only via dissociative recombi-

via Equation (11). Column densities, equivalent widths, velocity FWHM, and interstellar gas velocities for all of the sight lines presented in Figures 1–13 are reported in Table 2.
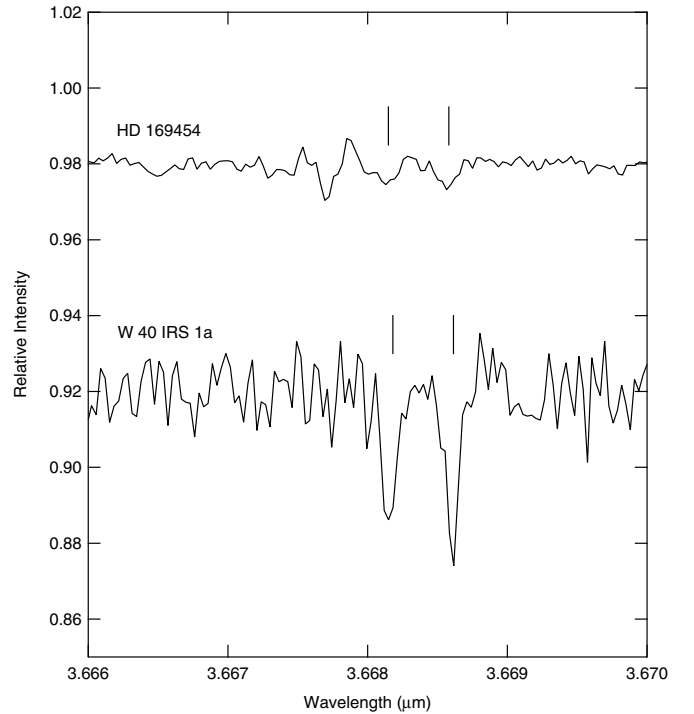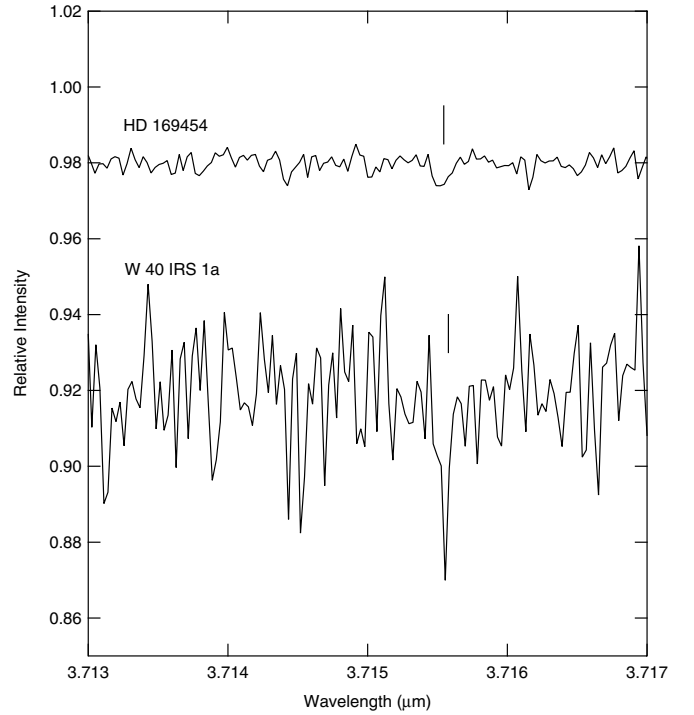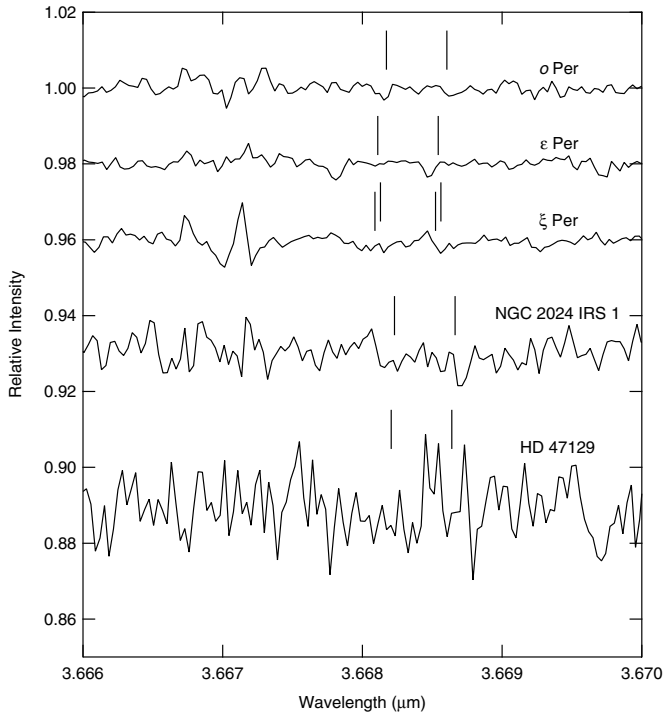
Figure 5. Same as Figure 1 except for the sight lines toward o Per, ε Per, ξ Per, NGC 2024 IRS 1, and HD 47129.

Figure 6. Same as Figure 1 except for the sight lines toward o Sco, HD 147888, HD 147889, ζ Oph, BD −14 5037, and HD 206267.
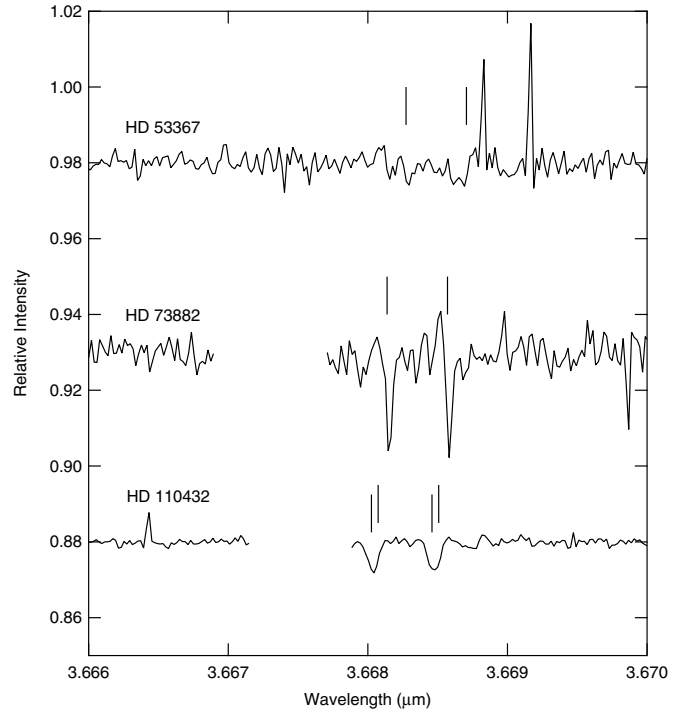

Figure 7. Same as Figure 1 except for the sight lines toward HD 53367, HD 73882, and HD 110432. Observations were made with CRIRES at VLT.
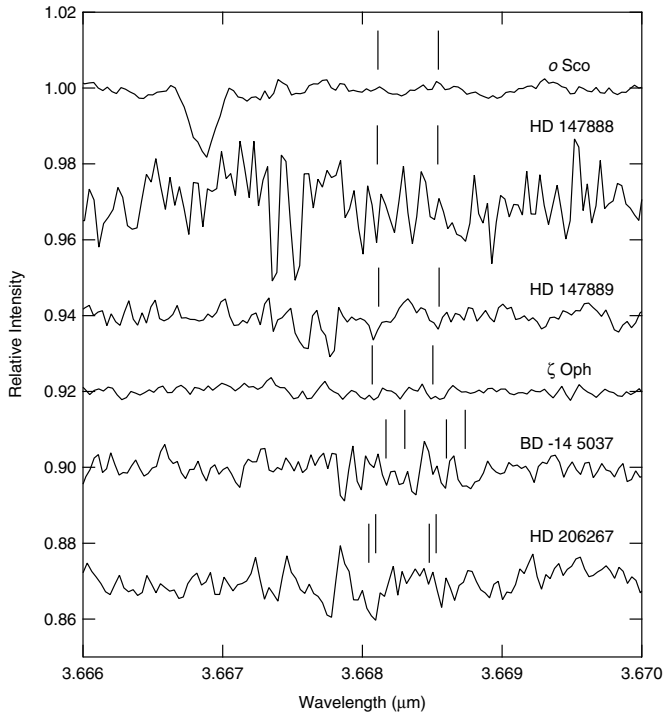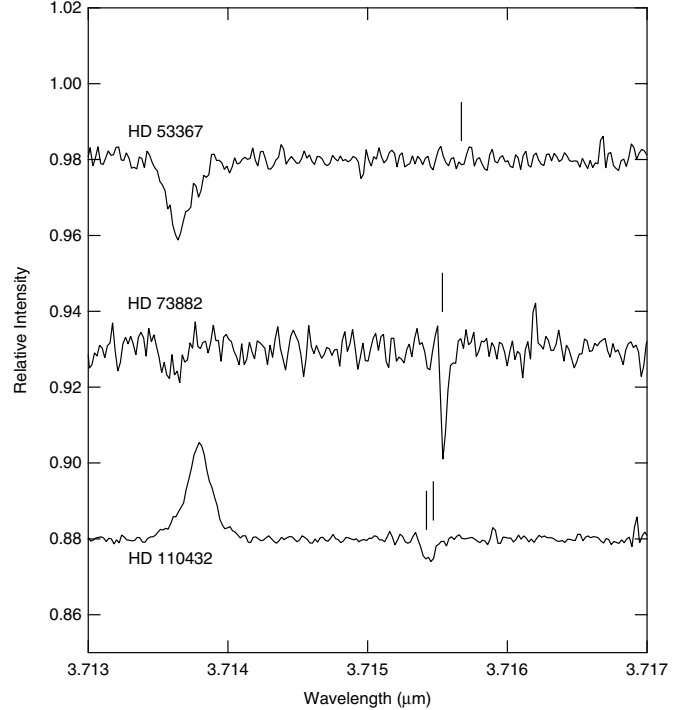

Figure 8. Same as Figure 7 except targeting the $R(1, 1)^l$ transition.

nation with electrons—the result is

$$\zeta_2 n(\mathrm{H}_2) = k_e n(\mathrm{H}_3^+) n_e, \tag{13}$$

where ζ_2 is the ionization rate of H_2, n's are number densities, and k_e is the H_3^+–electron recombination rate coefficient (see Table 3). Substituting the electron fraction (defined as $x_e \equiv n_e/n_\mathrm{H}$, where $n_\mathrm{H} \equiv n(\mathrm{H}) + 2n(\mathrm{H}_2)$) into Equation (13) and

solving for the ionization rate gives

$$\zeta_2 = k_e x_e n_\mathrm{H} \frac{n(\mathrm{H}_3^+)}{n(\mathrm{H}_2)}. \tag{14}$$

Observations cannot measure changes in these parameters along a line of sight, so we assume a uniform cloud with path length L and constant x_e, k_e, n_H, and $n(\mathrm{H}_3^+)/n(\mathrm{H}_2)$. In this case, the H_3^+ and H_2 densities can by definition be replaced with $N(\mathrm{H}_3^+)/L$
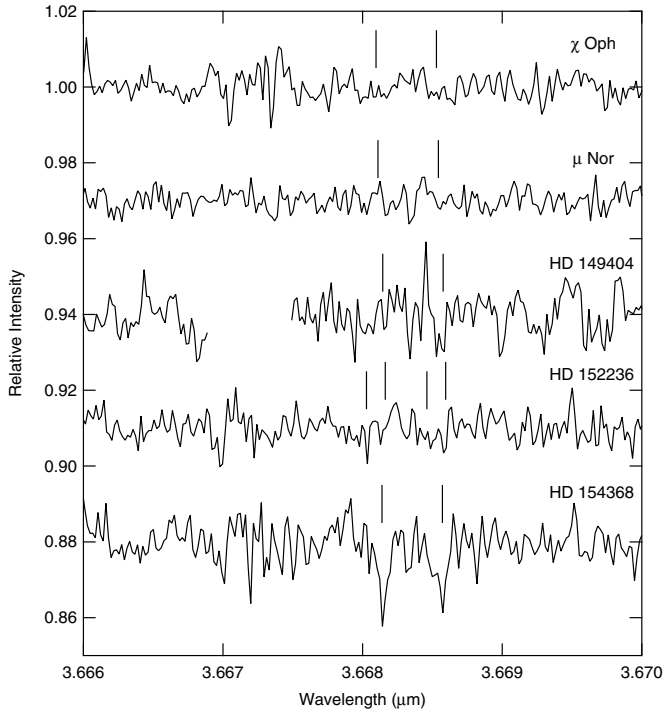
Figure 9. Same as Figure 1 except for the sight lines toward χ Oph, μ Nor, HD 149404, HD 152236, and HD 154368. Observations were made with Phoenix at Gemini South.
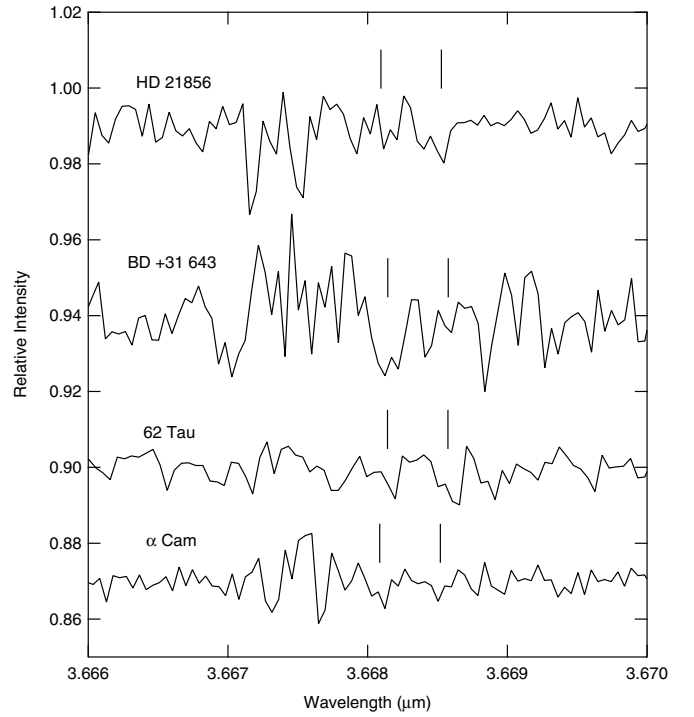

Figure 11. Same as Figure 1 except for the sight lines toward HD 21856, BD +31 643, 62 Tau, and α Cam. Observations were made with NIRSPEC at Keck.
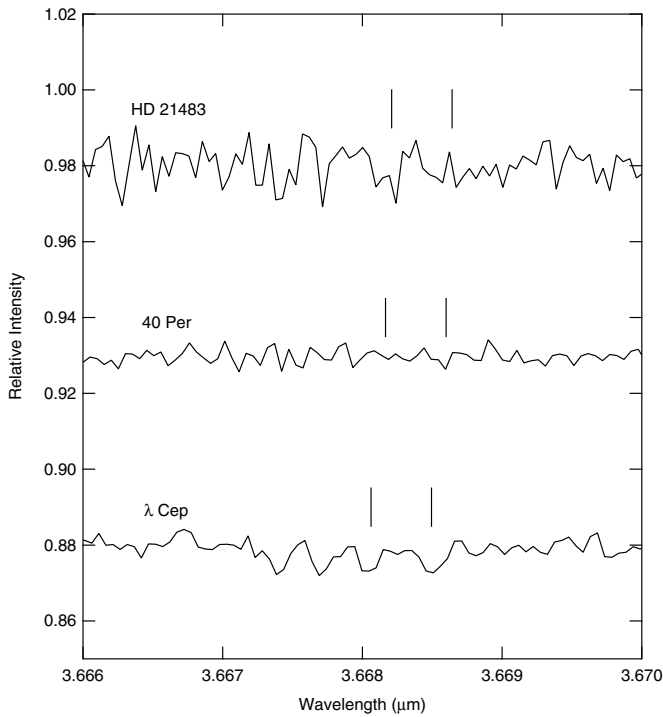

Figure 10. Same as Figure 1 except for the sight lines toward HD 21483, 40 Per, and λ Cep. Spectra combined observations using CGS4 at UKIRT and NIRSPEC at Keck.
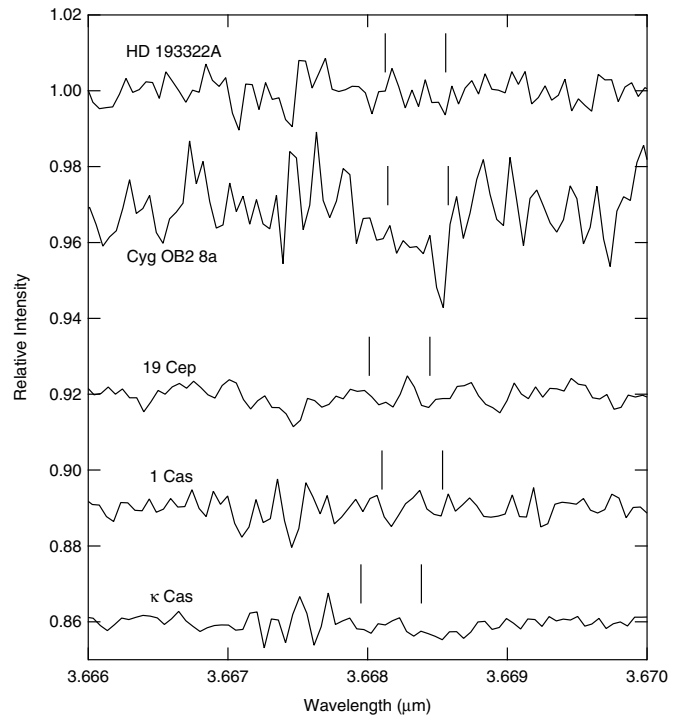
Figure 12. Same as Figure 11 except for the sight lines toward HD 193322A, Cyg OB2 8A, 19 Cep, 1 Cas, and κ Cas.

and $N(H_2)/L$, respectively, such that

$$\zeta_2 = k_e x_e n_H \frac{N(H_3^+)}{N(H_2)} \qquad (15)$$

gives the cosmic-ray ionization rate in a diffuse molecular cloud.

While Equation (15) only considers one formation and destruction mechanism for H_3^+, comparison to a more complete chemical reaction network shows that it is a robust approximation given diffuse cloud conditions. Assuming steady state for H_2^+ where destruction by electron recombination and charge transfer to protons (reactions (3) and (4)) are considered, and steady state for H_3^+ where destruction by proton transfer to CO

Table 2
Absorption Line Parameters

Object	Transition	v_{LSR} (km s^{-1})	FWHM (km s^{-1})	W_λ (10^{-6} μm)	$\sigma(W_\lambda)$ (10^{-6} μm)	$N(J, K)$ (10^{13} cm^{-2})	$\sigma(N)$ (10^{13} cm^{-2})
HD 20041	$R(1, 1)^u$	2.5	11.0	2.49	0.45	10.3	1.87
	$R(1, 0)$	−0.9	10.1	3.03	0.41	7.67	1.04
HD 21389	$R(1, 1)^u$	0.2	13.3	1.20	0.19	4.98	0.79
	$R(1, 0)$	0.8	12.9	1.46	0.19	3.69	0.47
ζ Per	$R(1, 1)^u$	8.0	10.3	0.99	0.11	4.09	0.46
	$R(1, 0)$	8.4	8.7	0.86	0.10	2.17	0.25
	$R(3, 3)^l$	. . .	10	. . .	0.10	. . .	0.37
X Per	$R(1, 1)^u$	7.0	11.7	1.16	0.20	4.81	0.81
	$R(1, 0)$	6.3	9.4	1.00	0.17	2.53	0.43
HD 29647	$R(1, 1)^u$	8.0	8.6	1.62	0.21	6.72	0.88
	$R(1, 0)$	8.2	11.0	2.06	0.26	5.21	0.67
HD 73882	$R(1, 1)^u$	5.9	3.9	1.44	0.21	5.97	0.86
	$R(1, 0)$	5.7	3.2	1.16	0.19	2.94	0.48
	$R(1, 1)^l$	5.4	3.5	1.34	0.15	6.15	0.69
HD 110432	$R(1, 1)^u$	−3.8	6.9	0.74	0.06	3.08	0.24
	$R(1, 0)$	−3.3	7.5	0.83	0.07	2.11	0.17
	$R(1, 1)^l$	−3.1	8.1	0.69	0.06	3.15	0.28
HD 154368	$R(1, 1)^u$	5.4	5.8	1.57	0.28	6.51	1.16
	$R(1, 0)$	4.6	5.1	1.13	0.25	2.86	0.63
HD 168607	$R(1, 1)^u$	20.9	7.9	1.07	0.13	4.44	0.53
	$R(1, 0)$	22.4	8.9	0.85	0.14	2.16	0.34
HD 168625	$R(1, 1)^u$	19.5	9.5	1.58	0.19	6.55	0.78
	$R(1, 0)$	22.0	9.1	1.59	0.19	4.02	0.48
HD 169454	$R(1, 1)^u$	4.5	10.6	0.80	0.12	3.32	0.51
	$R(1, 0)$	4.0	11.7	1.01	0.12	2.56	0.30
	$R(1, 1)^l$	3.8	8.7	0.77	0.18	3.53	0.84
W40 IRS 1A	$R(1, 1)^u$	5.9	8.9	4.19	0.64	17.4	2.66
	$R(1, 0)$	7.4	7.8	4.48	0.60	11.3	1.51
	$R(1, 1)^l$	6.1	4.5	2.80	0.71	12.8	3.26
HD 229059	$R(1, 1)^u$	3.8	9.3	5.10	0.25	21.2	1.02
	$R(1, 0)$	3.5	9.7	6.42	0.26	16.2	0.65
HD 204827	$R(1, 1)^u$	−0.8	11.0	3.11	0.53	12.9	2.18
	$R(1, 0)$	−0.9	8.7	2.41	0.51	6.10	1.29
λ Cep	$R(1, 1)^u$	−2.9	10.7	1.04	0.23	4.31	0.95
	$R(1, 0)$	−1.4	13.5	1.29	0.27	3.26	0.67
κ Cas	$R(1, 1)^u$	. . .	15	. . .	0.19	. . .	0.77
	$R(1, 0)$	. . .	15	. . .	0.19	. . .	0.47
HD 21483	$R(1, 1)^u$	. . .	15	. . .	0.47	. . .	1.97
	$R(1, 0)$	. . .	15	. . .	0.47	. . .	1.20
HD 21856	$R(1, 1)^u$	. . .	15	. . .	0.46	. . .	1.92
	$R(1, 0)$	. . .	15	. . .	0.46	. . .	1.17
40 Per	$R(1, 1)^u$	. . .	15	. . .	0.18	. . .	0.74
	$R(1, 0)$	. . .	15	. . .	0.18	. . .	0.45
o Per	$R(1, 1)^u$	. . .	10	. . .	0.10	. . .	0.41
	$R(1, 0)$	. . .	10	. . .	0.10	. . .	0.25
BD +31 643	$R(1, 1)^u$	. . .	15	. . .	0.95	. . .	3.95
	$R(1, 0)$	. . .	15	. . .	0.95	. . .	2.41
ϵ Per	$R(1, 1)^u$	. . .	10	. . .	0.08	. . .	0.33
	$R(1, 0)$	. . .	10	. . .	0.08	. . .	0.20
ξ Per	$R(1, 1)^u$	. . .	10	. . .	0.11	. . .	0.44
	$R(1, 0)$	. . .	10	. . .	0.11	. . .	0.27
62 Tau	$R(1, 1)^u$	. . .	15	. . .	0.37	. . .	1.53
	$R(1, 0)$	. . .	15	. . .	0.37	. . .	0.93
α Cam	$R(1, 1)^u$	. . .	15	. . .	0.30	. . .	1.26
	$R(1, 0)$	. . .	15	. . .	0.30	. . .	0.77
NGC 2024 IRS1	$R(1, 1)^u$	. . .	10	. . .	0.26	. . .	1.09
	$R(1, 0)$	. . .	10	. . .	0.26	. . .	0.66
HD 47129	$R(1, 1)^u$	. . .	15	. . .	0.60	. . .	2.48
	$R(1, 0)$	. . .	15	. . .	0.60	. . .	1.51
HD 53367	$R(1, 1)^u$	. . .	5	. . .	0.12	. . .	0.50
	$R(1, 0)$	. . .	5	. . .	0.12	. . .	0.30
	$R(1, 1)^l$	. . .	5	. . .	0.07	. . .	0.32
o Sco	$R(1, 1)^u$	. . .	10	. . .	0.08	. . .	0.35
	$R(1, 0)$	. . .	10	. . .	0.08	. . .	0.21

Table 2
(Continued)

Object	Transition	v_{LSR} (km s^{-1})	FWHM (km s^{-1})	W_λ ($10^{-6}\,\mu$m)	$\sigma(W_\lambda)$ ($10^{-6}\,\mu$m)	$N(J, K)$ (10^{13} cm^{-2})	$\sigma(N)$ (10^{13} cm^{-2})
HD 147888	$R(1, 1)^u$	...	10	...	0.46	...	1.92
	$R(1, 0)$	...	10	...	0.46	...	1.17
HD 147889	$R(1, 1)^u$	...	10	...	0.18	...	0.74
	$R(1, 0)$	...	10	...	0.18	...	0.45
χ Oph	$R(1, 1)^u$	...	5	...	0.11	...	0.45
	$R(1, 0)$	...	5	...	0.11	...	0.27
μ Nor	$R(1, 1)^u$	...	5	...	0.12	...	0.49
	$R(1, 0)$	...	5	...	0.12	...	0.30
HD 149404	$R(1, 1)^u$	...	5	...	0.23	...	0.94
	$R(1, 0)$	...	5	...	0.23	...	0.57
ζ Oph	$R(1, 1)^u$	...	10	...	0.08	...	0.31
	$R(1, 0)$	...	10	...	0.08	...	0.19
HD 152236	$R(1, 1)^u$	...	5	...	0.14	...	0.59
	$R(1, 0)$	...	5	...	0.14	...	0.36
BD -14 5037	$R(1, 1)^u$	...	10	...	0.23	...	0.95
	$R(1, 0)$	...	10	...	0.23	...	0.58
HD 193322A	$R(1, 1)^u$	...	15	...	0.37	...	1.55
	$R(1, 0)$	...	15	...	0.37	...	0.95
Cyg OB2 8A	$R(1, 1)^u$	...	15	...	0.98	...	4.07
	$R(1, 0)$	...	15	...	0.98	...	2.48
HD 206267	$R(1, 1)^u$	...	10	...	0.30	...	1.25
	$R(1, 0)$	...	10	...	0.30	...	0.76
19 Cep	$R(1, 1)^u$	...	15	...	0.26	...	1.10
	$R(1, 0)$	...	15	...	0.26	...	0.67
1 Cas	$R(1, 1)^u$	...	15	...	0.29	...	1.21
	$R(1, 0)$	...	15	...	0.29	...	0.74

Notes. Columns 6 ($\sigma(W_\lambda)$) and 8 ($\sigma(N)$) are 1σ uncertainties on the equivalent width and column density, respectively. The FWHM values in the case of non-detections are appropriate for the resolution of the instrument used in each observation, and are used in computing the value of $\mathcal{N}_{pix}$ required in Equation (12).
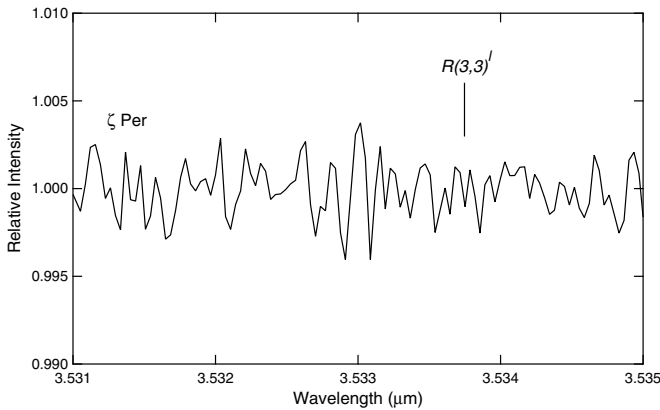

Figure 13. Spectrum covering the $R(3, 3)^l$ line of H_3^+ toward ζ Per taken with CGS4 at UKIRT. The vertical line marks the expected position of the absorption line. Absorption from the (3, 3) metastable state is not expected in the diffuse ISM, and thus far has only been detected in the Galactic center (Goto et al. 2002, 2008, 2011; Oka et al. 2005; Geballe & Oka 2010).

and O (reactions (6), (7), and (8)) is accounted for, gives the equations

$$\zeta_2 n(H_2) = k_3 n_e n(H_2^+) + k_4 n(H) n(H_2^+) + k_2 n(H_2) n(H_2^+), \quad (16)$$

$$k_2 n(H_2) n(H_2^+) = k_e n_e n(H_3^+) + k_{CO} n(CO) n(H_3^+) + k_O n(O) n(H_3^+). \quad (17)$$

Solving for the ionization rate and making similar substitutions as before results in

$$\zeta_2 = \frac{N(H_3^+)}{N(H_2)} n_H \left[k_e x_e + k_{CO} x(CO) + k_O x(O) \right]$$
$$\times \left[1 + \frac{2k_3 x_e}{k_2 f_{H_2}} + \frac{2k_4}{k_2} \left(\frac{1}{f_{H_2}} - 1 \right) \right], \quad (18)$$

where relevant rate coefficients are given in Table 3, $k_{CO} = k_6 + k_7$, and $f_{H_2} \equiv 2n(H_2)/n_H$ is the fraction of hydrogen nuclei in molecular form.

The cosmic-ray ionization rate as a function of electron fraction is plotted in Figure 14 for both Equations (15) and (18). In all four panels, the thick solid line shows the linear relationship given by Equation (15), while the various other curves show the ionization rate determined using Equation (18) and different values of $x(CO)$, $x(O)$, and f_{H_2}. In the first panel $x(CO)$ is set to 10^{-6}, 10^{-5}, and 10^{-4} with $x(O) = 10^{-8}$ and $f_{H_2} = 1$. In the second panel $x(O)$ is set to 10^{-6}, 10^{-5}, 10^{-4}, and 3×10^{-4} with $x(CO) = 10^{-8}$ and $f_{H_2} = 1$. In the third panel f_{H_2} is set to 0.67, 0.5, and 0.1 with $x(CO) = x(O) = 10^{-8}$.

The first and second panels show that Equation (18) only differs significantly from Equation (15) when $x_e \lesssim 10^{-5}$, and for high fractional abundances of CO and O ($\gtrsim 10^{-4}$). These deviations occur when proton transfer to CO and O comes to dominate over electron recombination as the primary destruction pathways for H_3^+. The third panel shows that f_{H_2} affects the ionization rate for all values of x_e, but that rather low molecular hydrogen fractions are necessary to significantly alter the inferred value of ζ_2. With $f_{H_2} = 0.5$ (i.e., twice as many H
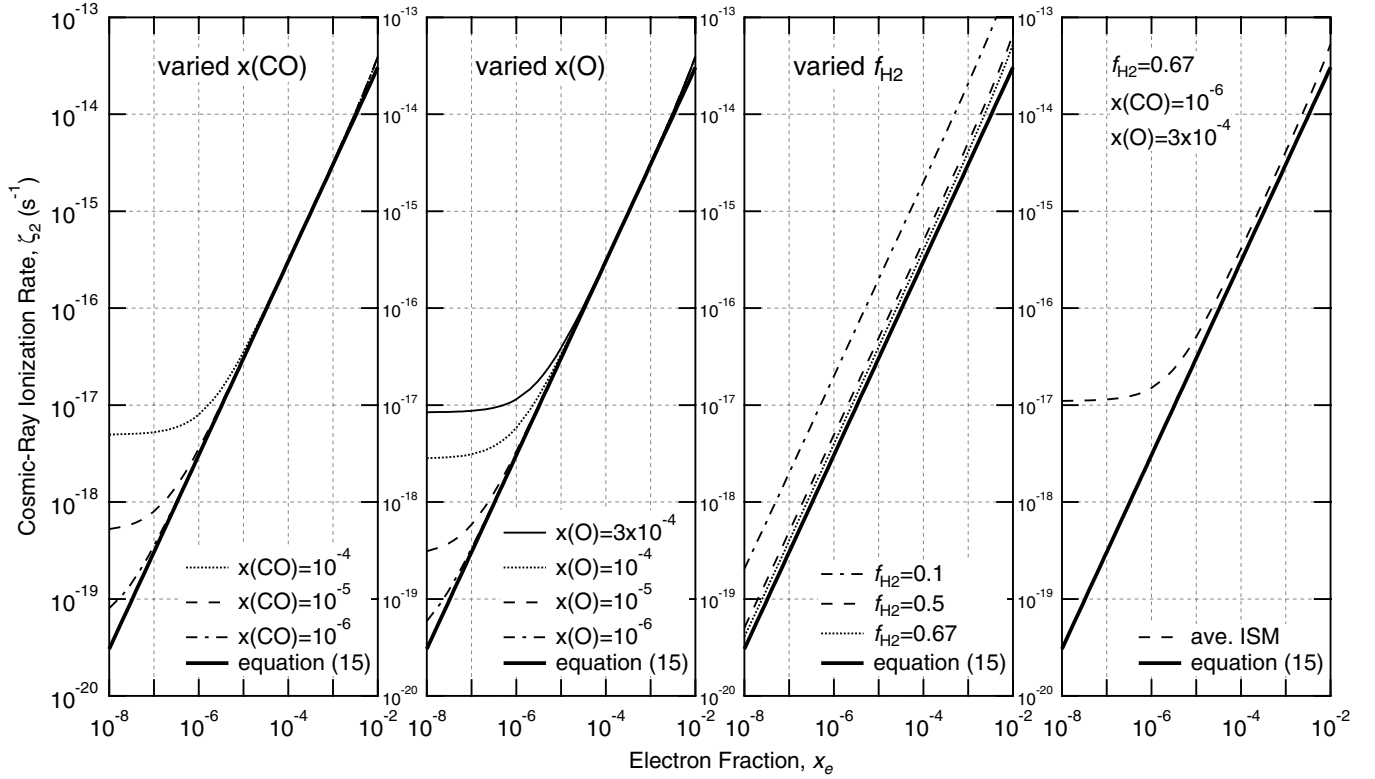
Figure 14. Cosmic-ray ionization rate (ζ_2) as a function of the electron fraction (x_e) for simplified chemistry (Equation (15)) and more complete chemistry (Equation (18)). In all cases $n_H = 200$ cm^{-3}, $N(H_3^+)/N(H_2) = 10^{-7}$, and $T = 70$ K. The thick solid line shows the linear approximation given by Equation (15). The first panel shows the result of varying $x(CO)$, with $x(O) = 10^{-8}$ and $f_{H_2} = 1$; the second panel shows the result of varying $x(O)$, with $x(CO) = 10^{-8}$ and $f_{H_2} = 1$; the third panel shows the result of varying f_{H_2}, with $x(CO) = 10^{-8}$ and $x(O) = 10^{-8}$; the last panel shows Equation (18) for average diffuse ISM conditions ($f_{H_2} = 0.67$, $x(CO) = 10^{-6}$, $x(O) = 3 \times 10^{-4}$). At $x_e = 1.5 \times 10^{-4}$, Equation (18) gives an ionization rate 1.33 times larger than Equation (15), so if anything, we are slightly underestimating ζ_2.

Table 3
Rate Coefficients for Reactions Involved in H$_3^+$ Chemistry

Reaction	Rate Coefficient (cm^3 s^{-1})	Reference
$H_2^+ + H_2 \rightarrow H_3^+ + H$	$k_2 = 2.08 \times 10^{-9}$	1
$H_2^+ + e^- \rightarrow H + H$	$k_3 = 1.6 \times 10^{-8}(T/300)^{-0.43}$	2
$H_2^+ + H \rightarrow H_2 + H^+$	$k_4 = 6.4 \times 10^{-10}$	3
$H_3^+ + e^- \rightarrow$ products	$k_5 = k_e = -1.3 \times 10^{-8} + 1.27 \times 10^{-6} T_e^{-0.48}$	4
$H_3^+ + CO \rightarrow H_2 + HCO^+$	$k_6 = 1.36 \times 10^{-9}(T/300)^{-0.142} \exp(3.41/T)$	5
$H_3^+ + CO \rightarrow H_2 + HOC^+$	$k_7 = 8.49 \times 10^{-10}(T/300)^{0.0661} \exp(-5.21/T)$	5
$H_3^+ + O \rightarrow H_2 + OH^+$	$k_8 = k_O = 1.14 \times 10^{-9}(T/300)^{-0.156} \exp(-1.41/T)$	5
$H_3^+ + N_2 \rightarrow H_2 + HN_2^+$	$k_9 = 1.8 \times 10^{-9}$	6

Notes. Numerical subscripts on the rate coefficients refer to the corresponding reaction numbers given in the text. The H$_3^+$–electron recombination rate coefficient, k_5, is referred to as k_e throughout the text. The rate coefficient for destruction via proton transfer to CO used in the text, k_{CO}, is equal to $k_6 + k_7$. The rate coefficient for destruction via proton transfer to O, k_8, is referred to as k_O throughout the text. All temperature-dependent coefficients are in terms of the gas kinetic temperature, T, except for k_e, which is in terms of the electron temperature, T_e. However, it is expected that electrons and H$_2$ should be thermalized to the gas kinetic temperature via collisions, so we make no distinction between T_e, T_{01}, and T in our calculations.
References. (1) Theard & Huntress 1974; (2) Mitchell 1990; (3) Karpas et al. 1979; (4) McCall et al. 2004; (5) Klippenstein et al. 2010; (6) Rakshit 1982.

atoms as H$_2$ molecules) the value given by Equation (18) is about 1.6 times that from Equation (15), while for $f_{H_2} = 0.67$ (i.e., equal number of H and H$_2$) the value given by Equation (18) is about 1.3 times that from Equation (15). This deviation is caused by the larger relative abundance of atomic hydrogen destroying H$_2^+$ before it can form H$_3^+$, and is represented by the final term in Equation (18). The destruction of H$_2^+$ by electron recombination does not play a major role in the chemical network used here,

and its influence can only be seen in the slight deviation between Equations (15) and (18) when $x_e \sim 10^{-2}$.

Although some of the sight lines studied herein have molecular hydrogen fractions of $f_{H_2} = 0.2$ as determined from observations of H and H$_2$ (Savage et al. 1977; Rachford et al. 2002, 2009), it must be remembered that these are line-of-sight fractions, while Equation (18) requires local fractions. As it is expected that there will be atomic gas along a line of sight that

is not associated with a cloud containing H_2, the line-of-sight value of f_{H_2} *always* underestimates the value of f_{H_2} within a diffuse molecular cloud. It is generally assumed that the interior of a diffuse molecular cloud has conditions where $0.67 < f_{H_2} < 1$ (i.e., somewhere between half and all of the hydrogen is in molecular form), such that reaction (4) will not be very important.

Using average diffuse molecular cloud conditions ($x(O) = 3 \times 10^{-4}$, Cartledge et al. 2004 and Jensen et al. 2005; $x(CO) \sim 10^{-6}$, Sonnentrucker et al. 2007; $f_{H_2} \gtrsim 0.67$) in Equation (18) produces the dashed curve in the last panel of Figure 14, and at $x_e = x(C^+) = 1.5 \times 10^{-4}$ (Cardelli et al. 1996; Sofia et al. 2004) the resulting ionization rate is only 1.33 times larger than that inferred from Equation (15). This demonstrates that Equation (15) is a good approximation to Equation (18) in the regions we study, and so we adopt Equation (15) in computing ζ_2.

With Equation (15), the cosmic-ray ionization rate (ζ_2) can be determined from the H_3^+ column density ($N(H_3^+)$), H_2 column density ($N(H_2)$), total hydrogen density (n_H), electron fraction (x_e), and H_3^+–electron recombination rate coefficient (k_e). The electron fraction can be approximated by the fractional abundance of C^+ assuming that nearly all electrons are the result of singly photoionized carbon. In sight lines where C^+ has been observed, the measured value of $x(C^+)$ is used for x_e. For all other sight lines, the average fractional abundance measured in various diffuse clouds, $x(C^+) \approx 1.5 \times 10^{-4}$ (Cardelli et al. 1996; Sofia et al. 2004), is adopted for x_e. Uncertainties in x_e are assumed to be $\pm 20\%$, i.e., $\pm 3 \times 10^{-5}$. The H_3^+–electron recombination rate coefficient has now been measured in multiple laboratory experiments (e.g., McCall et al. 2004; Kreckel et al. 2005, 2010) with consistent results and is presented in Table 3. When available the spin temperature of H_2, T_{01}, and its uncertainty are used in calculating k_e; otherwise, an average value of 70 ± 10 K is adopted. The total hydrogen number density is difficult to determine, but various studies have estimated n_H using a rotational excitation analysis of observed C_2 lines (Sonnentrucker et al. 2007), an analysis of H and the $J = 4$ level of H_2 (Jura 1975), or a thermal pressure analysis of fine structure lines of C I (Jenkins et al. 1983). Number densities from these studies are presented in Table 4 when available. For sight lines without estimated densities, the rough average value of $n_H = 200$ cm^{-3} is adopted. In all cases, uncertainties in n_H are assumed to be $\pm 50\%$ of the reported values. Absorption lines from electronic transitions of H_2 have been observed in the UV along many of the sight lines in this study (from which the aforementioned values of T_{01} are derived; Savage et al. 1977; Rachford et al. 2002, 2009). In sight lines where H_2 has not been observed, two other methods were used to estimate $N(H_2)$. The preferred method uses column densities of CH determined from observations in combination with the relation $N(CH)/N(H_2) = 3.5^{+2.1}_{-1.4} \times 10^{-8}$ from Sheffer et al. (2008). In sight lines where neither H_2 nor CH has been observed, $N(H_2)$ is estimated from the color excess, $E(B - V)$, using the relation $N_H \approx E(B - V)5.8 \times 10^{21}$ cm^{-2} mag^{-1} from Bohlin et al. (1978), and assuming $f_{H_2} \approx 2N(H_2)/N_H = 0.67$. Molecular hydrogen column densities determined both from observations and estimates are presented in Table 4.

While Table 2 gives individual column densities for the lowest lying *ortho* and *para* levels of H_3^+, values of $N(H_3^+)$ in Table 4 are equal to the sum of the column densities in the (1, 1) and (1, 0) states (i.e., $N(H_3^+) = N(1, 1) + N(1, 0)$). In cases where observations of both the $R(1, 1)^u$ and $R(1, 1)^l$ lines produce

independent values of $N(1, 1)$, a variance weighted average,

$$N = \sum_{i=1}^{n} \left(N_i / \sigma_i^2 \right) / \sum_{i=1}^{n} \left(1/\sigma_i^2 \right), \quad (19)$$

is used to determine $N(1, 1)$. Because there are only two independent measurements of $N(1, 1)$, the uncertainty of the weighted average, $S[N(1, 1)]$, is determined using an unbiased estimator of a weighted population variance for small samples. This is given by

$$S^2 = \frac{V_1}{V_1^2 - V_2} \sum_{i=1}^{n} w_i (N_i - \mu^*)^2, \quad (20)$$

where

$$w_i = \frac{1}{\sigma_i^2}, V_1 = \sum_{i=1}^{n} w_i, V_2 = \sum_{i=1}^{n} w_i^2,$$

and μ^* is the weighted average determined from Equation (19). The uncertainty in the total H_3^+ column density is then computed as usual by adding $\sigma[N(1, 1)]$ and $\sigma[N(1, 0)]$ in quadrature. Upper limits to the H_3^+ column density should be taken as $3\sigma[N(H_3^+)]$.

Using Equation (15), and taking the values described above and in Table 4, cosmic-ray ionization rates are inferred for all diffuse molecular clouds where H_3^+ observations have been made. These values of ζ_2 are presented in Column 10 of Table 4, with uncertainties in Column 11. As for the H_3^+ column densities, upper limits to the cosmic-ray ionization rate should be taken as $3\sigma(\zeta_2)$.

For one sight line however, that toward NGC 2024 IRS 1, a different analysis is used because recent observations suggest that the interstellar material is more likely dense than diffuse (T. Snow 2011, private communication). In this case, values appropriate for dense clouds ($x_e = 10^{-7}$, $f_{H_2} = 1$) are adopted, effectively simplifying Equation (18) to

$$\zeta_2 = \frac{N(H_3^+)}{N(H_2)} n_H \left[k_{CO} x(CO) + k_O x(O) \right]. \quad (21)$$

The density and temperature are also set to average dense cloud values ($n_H = 10^4$ cm^{-3}, $T = 30$ K). The large CO column density ($N(CO) = 1.26 \times 10^{18}$ cm^{-2}; T. Snow 2011, private communication) results in $x(CO) = 1.28 \times 10^{-4}$, demonstrating that most of the carbon is in molecular form, and thus validating the low value of x_e assumed above. Oxygen abundances are typically about two times carbon abundances (Lodders 2003), such that half of all O is expected to be in the form of CO. We assume the remainder to be in atomic form, and use $x(O) = x(CO)$ in Equation (21). The resulting upper limit on the cosmic-ray ionization rate toward NGC 2024 IRS 1 is $\zeta_2 < 4.2 \times 10^{-17}$ s^{-1}. This lower value is expected in dense cloud conditions, as will be discussed below, and is excluded from our analysis of the distribution of ionization rates in diffuse clouds.

5.3. The Distribution of Cosmic-ray Ionization Rates in Diffuse Clouds

With ionization rates and upper limits inferred for 50 diffuse cloud sight lines, it is interesting to study the distribution of our entire sample. Cosmic-ray ionization rates with 1σ uncertainties and 3σ upper limits are plotted in Figure 15. In order to find

Table 4
Cosmic-ray Ionization Rates

Object	$N(H_3^+)$ $(10^{13}$ cm$^{-2})$	$\sigma[N(H_3^+)]$ $(10^{13}$ cm$^{-2})$	H_3^+ Reference	$N(H_2)$ $(10^{20}$ cm$^{-2})$	$\sigma[N(H_2)]$ $(10^{20}$ cm$^{-2})$	H_2 Reference	n_H (cm^{-3})	Density Reference	ζ_2 $(10^{-16}$ s$^{-1})$	$\sigma(\zeta_2)$ $(10^{-16}$ s$^{-1})$
HD 20041	23.7	5.13	1,2	11.4	6.24	5	200		9.48	7.59
HD 21389	8.67	0.92	1	5.57	3.06	5	200		7.11	5.54
ζ Per	6.26	0.52	1	4.75	0.95	6	215	10	5.55	3.18
X Per	7.34	0.92	1	8.38	0.89	7	325	10	5.85	3.54
HD 29647	11.9	1.11	1	22.9	12.5	5	200		2.38	1.85
HD 73882	9.02	0.50	3	12.9	2.39	7	520	10	9.71	5.57
HD 110432	5.22	0.17	3	4.37	0.29	7	140	10	3.86	2.10
HD 154368	9.37	1.32	1	14.4	3.99	7	240	10	4.19	2.62
WR 104	23.2	1.54	2	44.7	22.3	8	200		2.37	1.76
HD 168607	6.60	0.63	1	17.4	8.47	5	200		1.73	1.28
HD 168625	10.6	0.92	1	16.3	7.95	5	200		2.96	2.17
HD 169454	5.93	0.34	1	16.6	8.37	5	300	10	2.45	1.83
W40 IRS 1A	26.9	3.54	1	56.3	28.2	8	300	11	3.27	2.45
WR 118 (5)	29.4	7.07	2	43.3	21.7	8	200		3.10	2.41
WR 118 (47)	30.8	5.73	2	45.5	22.7	8	200		3.10	2.36
WR 121	22.0	2.60	2	34.0	17.0	8	200		2.96	2.21
HD 183143 (7)	11.3	2.98	2	4.86	2.38	5	200		10.6	8.23
HD 183143 (24)	13.5	2.81	2	7.91	3.85	5	200		7.82	5.93
HD 229059	37.4	1.20	1	65.7	51.2	5	200		2.60	2.47
Cyg OB2 5	24.0	3.29	2	15.2	7.39	5	225	10	8.13	6.03
Cyg OB2 12	34.3	5.89	2,4	80.0	69.1	5	300	10	2.93	3.04
HD 204827	19.0	2.54	1	20.9	10.2	5	450	10	9.32	6.92
λ Cep	7.58	1.17	1	6.88	0.48	7	115	10	2.84	1.61
κ Cas	...	0.91	1	1.88	0.20	6	200		...	1.78
HD 21483	...	2.30	1	11.9	5.91	5	200		...	0.88
HD 21856	...	2.25	1	1.10	0.12	6	200		...	8.42
40 Per	...	0.87	1	2.92	0.53	6	80	12	...	0.57
o Per	...	0.47	1	4.09	0.79	6	265	10	...	0.85
BD +31 643	...	4.63	1	12.4	4.39	7	200		...	1.67
ϵ Per	...	0.38	1	0.33	0.07	6	15	13	...	0.36
ξ Per	...	0.51	1	3.42	0.53	6	300	13	...	1.98
62 Tau	...	1.79	1	6.23	1.12	7	280	10	...	2.06
α Cam	...	1.48	1	2.17	0.26	6	150	13	...	2.17
χ^2 Ori	...	2.75	2	4.90	1.05	9	200		...	2.79
HD 47129	...	2.91	1	3.51	0.58	6	200		...	3.81
HD 53367	...	0.44	1	11.1	1.44	9	200		...	0.20
o Sco	...	0.41	1	19.1	9.81	5	225	10	...	0.11
HD 147888	...	2.25	1	2.97	0.61	9	215	10	...	9.25
HD 147889	...	0.87	1	28.8	14.0	5	525	10	...	0.36
χ Oph	...	0.52	1	4.26	1.02	6	185	10	...	0.64
μ Nor	...	0.58	1	2.77	0.49	6	200		...	1.09
HD 149404	...	1.10	1	6.17	0.53	9	200		...	0.87
ζ Oph	...	0.37	1,2	4.49	0.42	6	215	10	...	0.39
HD 152236	...	0.69	1	5.34	1.32	9	200		...	0.63
BD -14 5037	...	1.11	1	38.6	23.6	5	200		...	0.13
P Cygni	...	1.84	2	3.14	1.61	5	200		...	2.67
HD 193322A	...	1.82	1	1.21	0.18	6	200		...	6.52
HD 194279	...	4.59	2	23.7	11.9	8	200		...	0.88
Cyg OB2 8A	...	4.77	1	9.26	4.58	5	200		...	2.35
HD 206267	...	1.47	1	7.18	0.59	7	200		...	0.97
19 Cep	...	1.28	1	1.21	0.18	6	200		...	4.60
1 Cas	...	1.41	1	1.40	0.19	6	200		...	4.18
NGC 2024 IRS 1	...	1.27	1	49.0	24.5	8	10000		...	0.14

Notes. The sight lines toward WR 118 and HD 183143 have two distinct velocity components observed in H_3^+ by McCall et al. (2002), and each of these components is labeled with a number in parentheses that corresponds to its average LSR velocity. When no reference for n_H was available the value was set to 200 cm^{-3}, an average density for diffuse molecular clouds. Upper limits to the cosmic-ray ionization rate should be taken as three times $\sigma(\zeta_2)$.
H_3^+ **References.** (1) This work; (2) McCall et al. 2002; (3) Crabtree et al. 2011; (4) McCall et al. 1998.
H_2 **References.** (5) Calculated from CH column densities using the relation $N(CH)/N(H_2) = 3.5^{+2.1}_{-1.4} \times 10^{-8}$ from Sheffer et al. (2008); (6) Savage et al. 1977; (7) Rachford et al. 2002; (8) calculated from $E(B-V)$ (see Table 1) using the relation $N_H \approx E(B-V)5.8 \times 10^{21}$ cm^{-2} mag^{-1} from Bohlin et al. (1978), and assuming $2N(H_2)/N_H = f_{H_2} = 0.67$; (9) Rachford et al. 2009.
n_H **References.** (10) Sonnentrucker et al. 2007; (11) Shuping et al. 1999; (12) Jenkins et al. 1983; (13) Jura 1975.
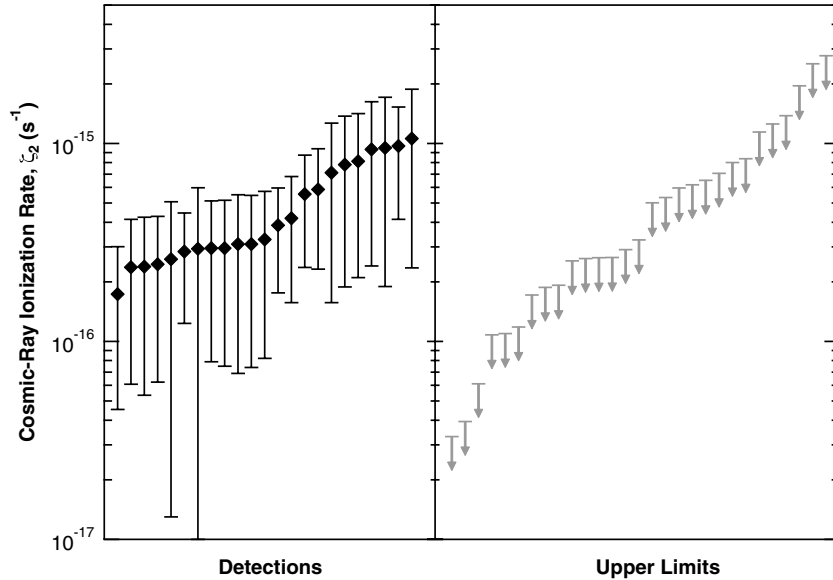
Figure 15. Cosmic-ray ionization rates and upper limits from the sample of diffuse cloud sight lines. The left panel shows ionization rates inferred from detections of H_3^+ with 1σ uncertainties. Points are spread out horizontally for clarity. The right panel shows 3σ upper limits to the ionization rate inferred for sight lines where H_3^+ is not detected. Some of the 3σ upper limits suggest ionization rates lower than those inferred in sight lines with H_3^+ detections. This likely points to variations in the cosmic-ray ionization rate between sight lines.

the probability density function for the cosmic-ray ionization rate in our sample, all of these data points are combined. Each sight line with an H_3^+ detection is treated as a Gaussian function with mean and standard deviation equal to the ionization rate and uncertainty reported in Columns 10 and 11 of Table 4. Each sight line with a non-detection of H_3^+ is treated as a Gaussian function with mean equal to zero and standard deviation equal to the uncertainty in Column 11 of Table 4. The cosmic-ray ionization rate cannot be negative, and it is reasonable to assume that in diffuse clouds there is some "floor" value below which ζ_2 does not fall caused by the continuous diffusion of particles throughout the Galactic disk (Webber 1998). We set this floor value to 10^{-17} s^{-1}—a rough average of ionization rates computed from proposed local interstellar proton spectra (e.g., Spitzer & Tomasko 1968; Webber 1998)—and truncate all of the Gaussian functions at this floor.[6] Each function is then re-normalized so that the area under the curve above the floor ionization rate is equal to 1. The truncated Gaussians are added together, and the final distribution is again normalized to have an area equal to 1.

The resulting probability density function, $f(\zeta_2)$, is plotted in the top panel of Figure 16. Because of the logarithmic x-axis, it is difficult to tell "by eye" which ionization rates are most probable. However, this is easily seen by scaling $f(\zeta_2)$ by ζ_2, as shown in the middle panel of Figure 16. By integrating $\zeta_2 f(\zeta_2)$, we find the mean value of the cosmic-ray ionization rate to be 3.5×10^{-16} s^{-1}, marked by the vertical dashed line. The minimum range of ionization rates (in log space) that contains 68.3% (Gaussian 1σ equivalent) of the area under $f(\zeta_2)$ is bounded by 5.0×10^{-17} s^{-1} on the left and 8.8×10^{-16} s^{-1} on the right, and is shown by the shaded region. The bottom panel of Figure 16 shows the cumulative distribution function, $F(\zeta_2)$, which gives the probability that the ionization rate is below a particular value.

6. CORRELATIONS BETWEEN LINE-OF-SIGHT PROPERTIES

6.1. The H_3^+ Column Density

Given that the H_3^+ formation process starts with H_2, one might expect that abundances of the two species should be correlated. Figure 17 shows $N(H_3^+)$ versus $N(H_2)$ for the entire sample of sight lines studied herein. Also included are H_3^+ column densities in sight lines near the supernova remnant IC 443 (Indriolo et al. 2010), as well as in dense clouds (McCall et al. 1999; Kulesa 2002; Brittain et al. 2004; Gibb et al. 2010). It is clear that for diffuse cloud sight lines where H_3^+ has been detected, relative abundances tend to cluster about 10^{-7}. A re-arrangement of Equation (15),

$$\frac{N(H_3^+)}{N(H_2)} = \frac{\zeta_2}{k_e x_e n_H},$$

suggests that scatter about a central value of $N(H_3^+)/N(H_2)$ is likely due to variations in ζ_2 and electron density ($x_e n_H$) between sight lines.

The much lower value of $N(H_3^+)/N(H_2)$ in dense clouds (10^{-8} to 10^{-9}) is the result of a higher density, different destruction partner, and lower ionization rate. Replacing electrons with CO as the dominant destruction partner leaves $N(H_3^+)/N(H_2)$ inversely proportional to $k_{CO}x(CO)n_H$. The rate coefficient for destruction of H_3^+ by CO is about 2 orders of magnitude slower than by electrons (see Table 3), the density of dense clouds is about 2–3 orders of magnitude larger than diffuse clouds (Snow & McCall 2006), and the fractional abundance of electrons in diffuse clouds should be about equal to that of CO in dense clouds. This means that ζ_2 must be about 0–2 orders of magnitude lower in dense clouds than in diffuse clouds to produce the observed results, and several studies of ionized species in dense clouds support such a trend (e.g., van der Tak & van Dishoeck 2000; Kulesa 2002; Hezareh et al. 2008).
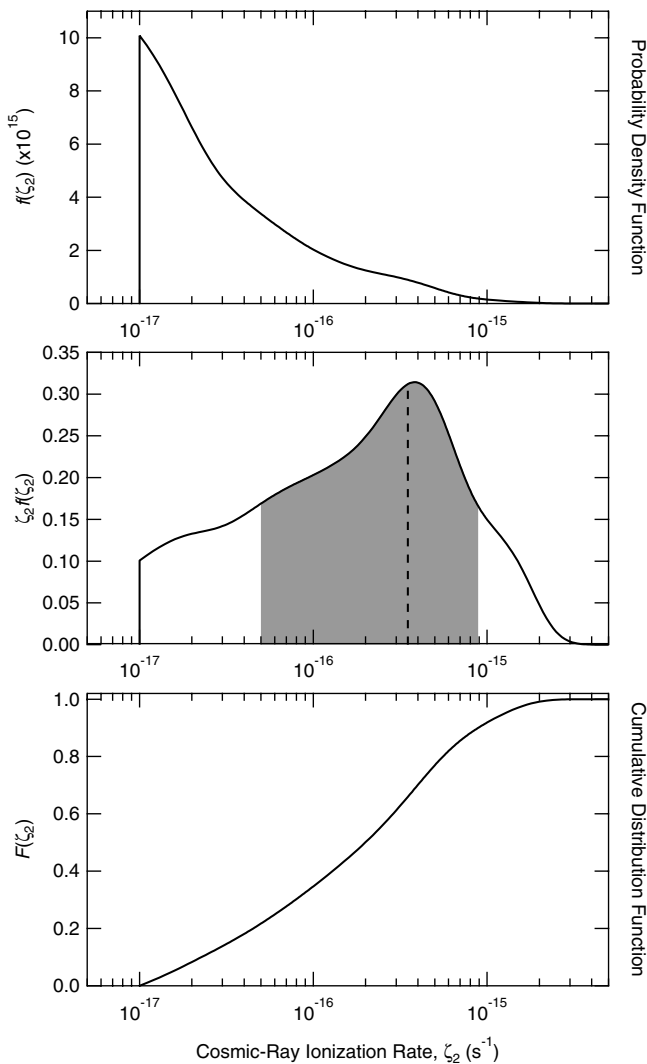
---

[6] Setting the floor ionization rate to zero does not significantly change our results.

Figure 16. Upper panel: probability density function, $f(\zeta_2)$, found by combining inferred ionization rates and upper limits. This is defined such that the probability of the cosmic-ray ionization rate being in any particular range is given by $P(a \leqslant \zeta_2 \leqslant b) = \int_a^b f(\zeta_2) d\zeta_2$. Center panel: probability density function multiplied by the ionization rate, $\zeta_2 f(\zeta_2)$. This allows one to see "by eye" what portion of $f(\zeta_2)$ carries the largest probability given the logarithmic x-axis. The vertical dashed line shows the mean value of $\zeta_2 = 3.5 \times 10^{-16}$ s^{-1}, and the shaded region is the smallest range of ionization rates in log space that contains 68.3% of the area under the probability density function. Lower panel: cumulative distribution function, $F(\zeta_2)$, showing the probability that ζ_2 is below any given value.

6.2. The Cosmic-ray Ionization Rate and Location

Beyond studying the cosmic-ray ionization rate in and of itself, it is insightful to search for correlations between ζ_2 and various other sight line parameters. One of the most fundamental relationships to study is that between ζ_2 and location within the Galaxy. The cosmic-ray ionization rate is plotted against Galactic longitude in the bottom panel of Figure 18. The top panel is a map in Galactic coordinates and the middle panel gives the distance to background sources such that the reader can easily trace the ionization rates in the bottom panel to an actual on-sky position. There are no apparent gradients in Figure 18, and comparisons of ζ_2 with both heliocentric distance and Galactocentric radius of background sources do not show any trends, thus suggesting that the mechanism responsible for variations in the cosmic-ray ionization rate does not operate on

large scales. To study variations of ζ_2 on small spatial scales, we investigate some of the closest sight line pairings from our data.

6.2.1. HD 168607 and HD 168625

The sight lines with the smallest angular separation in our survey are HD 168607 and HD 168625, separated by only 1″.1. The H$_3^+$ spectra for both targets are very similar (see Figure 2), suggesting that the absorption arises from a common cloud that must be in front of the closer target (HD 168607) at 1100 pc. At this distance, 1″.1 corresponds to an on-sky separation of 0.35 pc. Ionization rates for these two sight lines are consistent with each other within uncertainties, demonstrating uniformity of ζ_2 on the smallest spatial scales probed by our observations.

6.2.2. Cyg OB2 Association

Three of our target sight lines use stars in the Cyg OB2 association as background sources: Cyg OB2 5, Cyg OB2 12, and Cyg OB2 8A. Taking the OB association to be at 1.7 kpc (Torres-Dodgen et al. 1991), the on-sky distance between No. 5 and No. 12 is 2.6 pc, between No. 5 and No. 8A is 4.9 pc, and between No. 12 and No. 8A is 3.8 pc. Spectra toward No. 5 and No. 12 are somewhat similar, with components at about 6 km s^{-1} and 12 km s^{-1} LSR in a few molecular species (McCall et al. 2002). While the ionization rates in these two sight lines differ by about a factor of three, the inability to meaningfully separate the H$_3^+$ absorption features into the different velocity components makes this analysis very uncertain, and ζ_2 for Cyg OB2 5 and Cyg OB2 12 have overlapping 1σ uncertainties. Cyg OB2 8A, although not far removed from the other two sight lines, does not show H$_3^+$ absorption (see Figure 12), and may only contain the 6 km s^{-1} component (Snow et al. 2010). Still, the 3σ upper limit on ζ_2 toward No. 8A is consistent with the ionization rates inferred for the other two sight lines, and nothing conclusive can be drawn from this region.

A complementary method of tracing the cosmic-ray flux relies on γ-ray emission from π^0 decay, and observations of the Cygnus X region by *Fermi* Large Area Telescope (LAT) are suggestive of a large flux of recently accelerated hadronic cosmic rays (Ackermann et al. 2011) near the Cyg OB2 association. This is one of a few select regions where both γ-rays and H$_3^+$ have been observed, and presents the opportunity for a rather unique study based on both cosmic ray tracers. However, this analysis is beyond the scope of the current paper, and such a study would best be served by an expanded survey of H$_3^+$ that probes a larger extent of the gas traced by the γ-ray emission presented in Ackermann et al. (2011).

6.2.3. Per OB2 Association

The targets ζ Per, X Per, and o Per are all in the Perseus OB2 association (although the latter two may only be in the association by projection; de Zeeuw et al. 1999). X Per and ζ Per show very similar spectra (see Figure 1) with H$_3^+$ absorption lines at 7–8 km s^{-1} LSR, and the ionization rate inferred for each sight line is nearly identical. At a distance of 301 pc, the angular separation of 0°.88 corresponds to 4.6 pc in the plane of the sky. Among our targeted sight lines o Per is the next closest to these two, and, assuming a distance of 283 pc, is 10.5 pc away from ζ Per and 13.2 pc away from X Per. H$_3^+$ is not detected toward o Per, and the 3σ upper limit inferred for ζ_2 in this sight line is about equal to the lower 1σ bounds on the ionization rates toward X Per and ζ Per. While o Per is about 20 pc closer than

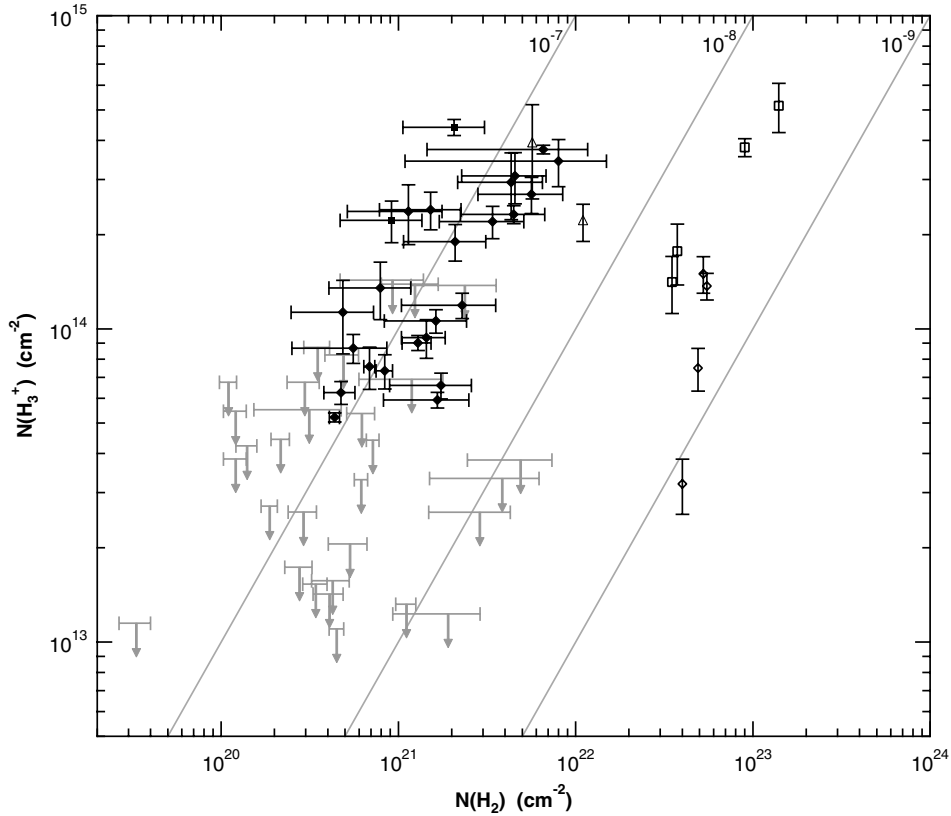**Figure 17.** $N(H_3^+)$ vs. $N(H_2)$ for diffuse clouds studied herein and various dense clouds reported in the literature. Symbols are as follows: filled diamonds—this study (detections); filled squares—Indriolo et al. (2010); gray arrows—this study (3σ upper limits on $N(H_3^+)$); open squares—McCall et al. (1999); open diamonds—Kulesa (2002); open triangles—Brittain et al. (2004) and Gibb et al. (2010). The diagonal lines show constant values of $N(H_3^+)/N(H_2)$ and are labeled accordingly. Diffuse clouds cluster about $N(H_3^+)/N(H_2) = 10^{-7}$, while dense clouds fall in the range between 10^{-8} and 10^{-9}. For diffuse cloud sight lines $N(H_2)$ is determined from UV H_2 observations, estimated from $N(CH)$, or estimated from $E(B-V)$, and values used here are presented in Table 4. For dense cloud sight lines $N(H_2)$ is determined from IR H_2 observations, estimated from A_V, or estimated from $N(CO)$.

ζ Per, the similar $E(B-V)$ values for both sight lines make it unlikely that we do not see H_3^+ simply because it is behind the target. Although not definitive, these results strongly suggest variations in the cosmic-ray ionization rate on a size scale of order 10 pc.

6.2.4. Ophiuchus–Scorpius Region

Many of our target sight lines probe the nearby Ophiuchus–Scorpius region, and some of the most closely spaced include o Sco, ρ Oph D, HD 147889, and χ Oph. The first three are all separated by 2–3 pc (assuming a distance of 136 pc), with χ Oph about 12–14 pc away. This is one of a few regions where H_3^+ is not detected in any of the target sight lines, and aside from ρ Oph D where the low continuum S/N level ($\sim$175) of the spectrum limits our analysis, the 3σ upper limits on ζ_2 are in the range $(3–19) \times 10^{-17}$ s^{-1}. These are some of the smaller inferred upper limits on ζ_2, and likely pertain to the material closest to the Sun probed in our survey as background sources are only 100–200 pc away. It is interesting then that these upper limits are consistent with the ionization rate of a few times 10^{-17} s^{-1} predicted by the local interstellar cosmic-ray spectrum (Webber 1998).

6.3. The Cosmic-ray Ionization Rate and Hydrogen Column Density

Given that there is no evidence for large-scale gradients in the cosmic-ray ionization rate, it is possible that properties of the observed clouds themselves are responsible for variations in ζ_2,

and will show some correlation with the cosmic-ray ionization rate. A parameter with which ζ_2 has been predicted to vary is the hydrogen column density, N_H (Padovani et al. 2009). This is because the energy spectrum of cosmic rays is expected to change with depth into a cloud. Lower-energy particles—those most efficient at ionization—will lose all of their energy to ionization interactions in the outer regions of a cloud, leaving only higher-energy particles to ionize the cloud interior. As such, the ionization rate in a cloud interior should be lower than in a cloud exterior. Because lower-energy particles can operate through a larger portion of clouds with lower column densities (Cravens & Dalgarno 1978), it is expected that the inferred ζ_2 will decrease with increasing N_H. A plot of ζ_2 versus N_H (and equivalent $E(B-V)$) is shown in Figure 19. In sight lines with multiple distinct velocity components, the total line-of-sight N_H has been divided by the number of components to better approximate the size of each individual cloud. Included in Figure 19 are data from four dense cloud sight lines observed in H_3^+ by Kulesa (2002), five dense cloud sight lines observed in $H^{13}CO^+$ by van der Tak & van Dishoeck (2000), and one dense cloud sight line observed in $HCNH^+$ by Hezareh et al. (2008) for the purpose of extending the relationship to much higher N_H. There does not appear to be a correlation between ζ_2 and N_H when only the diffuse molecular cloud sight lines are considered. However, when the dense cloud ionization rates (most of which are of order a few times 10^{-17} s^{-1}) are included, it seems that ζ_2 does decrease in sight lines with higher column densities.
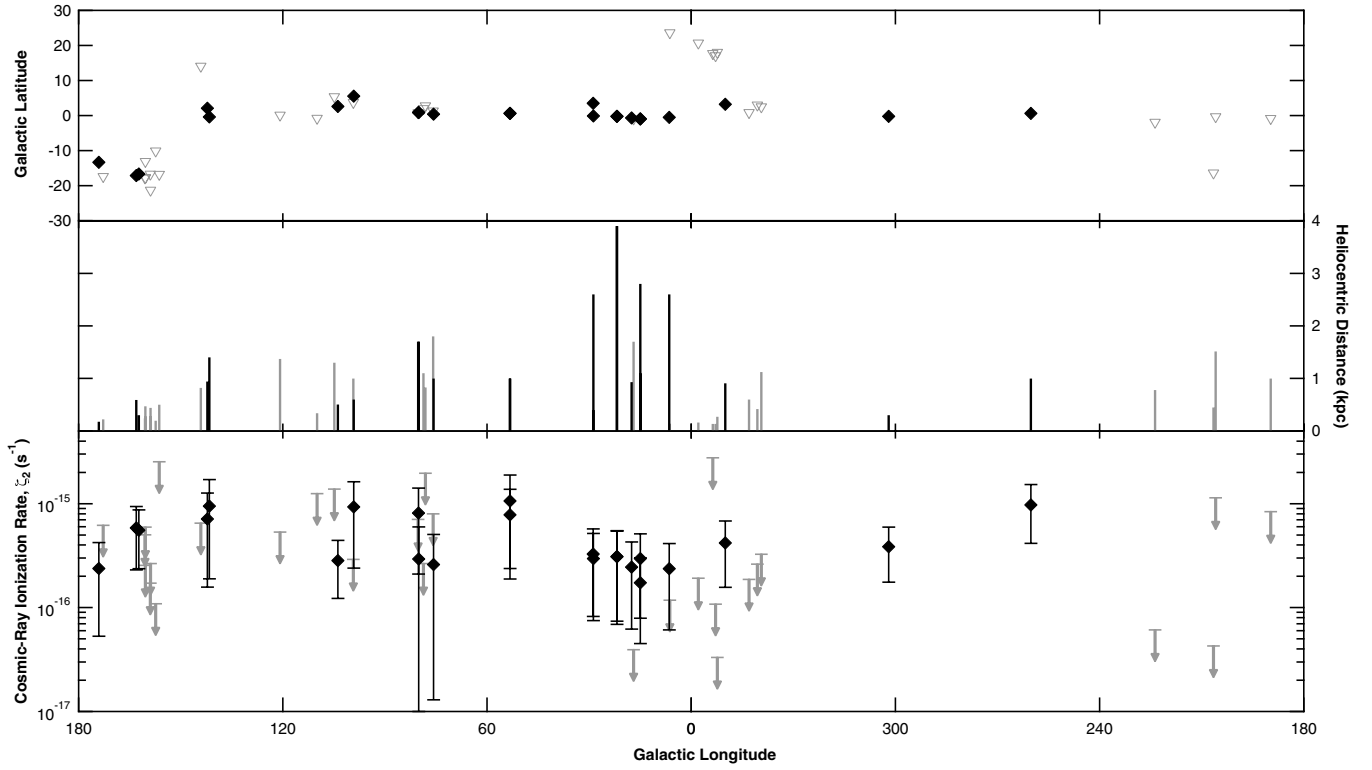
Figure 18. Top panel: map showing the locations of targeted sight lines in Galactic coordinates. Black diamonds mark sight lines where H_3^+ absorption is observed, and open gray triangles mark sight lines where H_3^+ is not detected. Middle panel: heliocentric distance of background sources with respect to Galactic longitude. Black lines mark sight lines where H_3^+ absorption is observed, and gray lines mark sight lines where H_3^+ is not detected. Bottom panel: the cosmic-ray ionization rate as a function of Galactic longitude. Black diamonds are inferred cosmic-ray ionization rates with 1σ uncertainties. Gray arrows are 3σ upper limits.
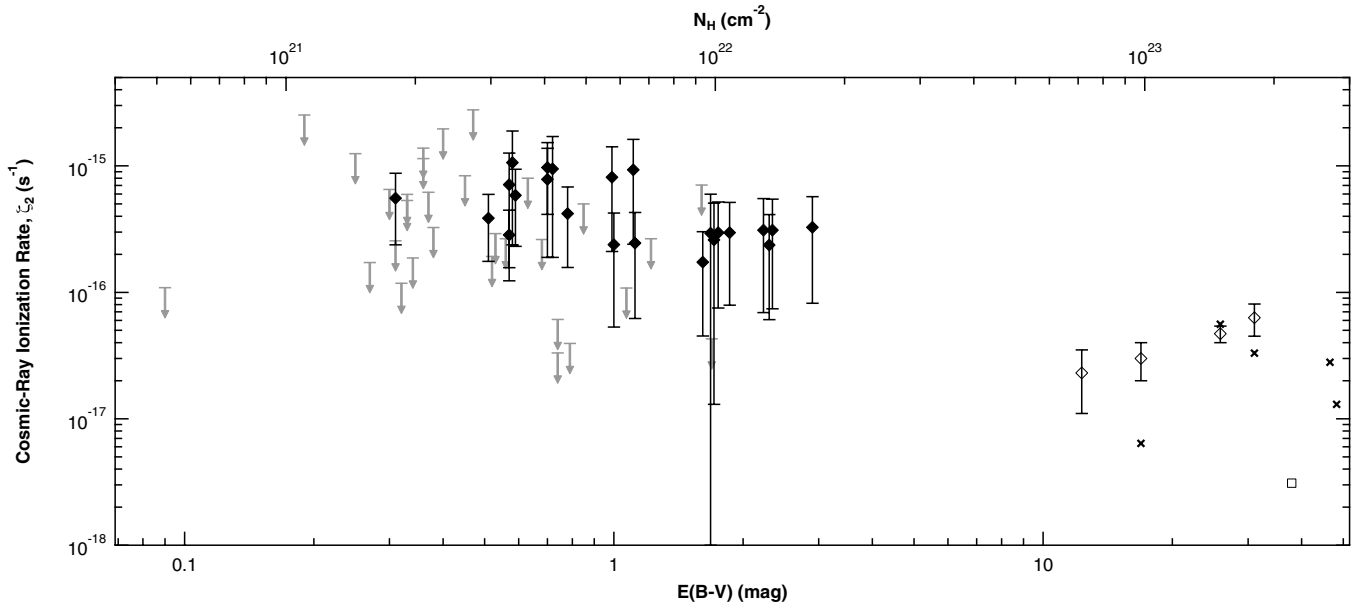
Figure 19. Cosmic-ray ionization rate as a function of cloud column density, N_H, and equivalent color excess, $E(B-V)$. For sight lines with multiple distinct velocity components, the total line-of-sight N_H has been divided by the number of cloud components. Filled diamonds are cosmic-ray ionization rates with 1σ uncertainties inferred for diffuse molecular clouds in this study. Gray arrows are 3σ upper limits from this study. Ionization rates inferred in dense clouds are as follows: open diamonds—H_3^+ observations of NGC 2024 IRS 2, AFGL 490, AFGL 2591, and AFGL 2136 by Kulesa (2002); crosses—HCO^+ observations of AFGL 2136, AFGL 2591, AFGL 490, W33 A, and W3 IRS 5 by van der Tak & van Dishoeck (2000); open square—$HCNH^+$ observation of DR 21(OH) by Hezareh et al. (2008). Various models (e.g., Padovani et al. 2009) predict that ζ_2 should decrease with increased N_H as low-energy cosmic rays lose all of their energy in the outer regions of a cloud. While no strong correlation is apparent from the diffuse cloud data alone, the addition of the dense cloud ionization rates from sight lines with much higher N_H does suggest such a trend.

7. DISCUSSION

Given that ζ_2 does *not* decrease with increased N_H among diffuse cloud sight lines, but does when switching from the diffuse to dense cloud regime, the following conclusions can be drawn. First, the cosmic rays that are primarily responsible for ionization in diffuse clouds must be able to propagate entirely through such clouds. This could easily be done by 10 MeV protons, which have a range of $Rn \approx 2 \times 10^{22}$ cm^{-2} (Cravens & Dalgarno 1978), about equal to the largest values of N_H in diffuse clouds studied here. However, a cloud with a large line-of-sight column density does not necessarily have a large column density in the plane of the sky. Even lower-energy particles then (e.g., 2 MeV protons with $Rn \approx 10^{21}$ cm^{-2}) could potentially cause ionization through the entire extent of an observed cloud.

Second, the cosmic rays that are responsible for most of the ionization in diffuse clouds must not be able to penetrate to the interiors of dense clouds. Again, something like 2–10 MeV protons fit this picture well. Most of the sight lines where H_3^+ is observed in dense clouds use embedded objects as background sources. Regions surrounding these sources have been mapped in various molecular species (via emission at radio wavelengths), implying large column densities in the plane of the sky in addition to the large column densities observed along the line of sight. This increases the likelihood that much of the material being probed is deep within the observed cloud.

Taken together, the higher ionization rates inferred in diffuse clouds and lower ionization rates inferred in dense clouds suggest that differences in ζ_2 can be explained by the inability of low-energy cosmic rays to penetrate large columns of material. However, under the assumption that the cosmic-ray spectrum is uniform throughout the Galactic disk (Webber 1998), this does not adequately explain differences in the cosmic-ray ionization rate amongst diffuse clouds. Instead, it would seem that the cosmic-ray spectrum—at least for particles in the energy range most efficient at ionization—must vary in space.

Despite the previously held assumption of a uniform cosmic-ray spectrum, it should not be surprising that the flux of low-energy particles varies across the Galaxy. Given a hydrogen density of 1 cm^{-3}, a 2 MeV proton will only travel about 320 pc (not necessarily in a straight line) before losing all of its energy, meaning that any point that is a few hundred parsecs away from a site of particle acceleration will not experience the same flux of 2 MeV protons as a point that is much closer to an acceleration site. For low-energy particles to even enter a diffuse cloud then, the cloud must be relatively close to a site of particle acceleration.

Regardless of where most low-energy cosmic rays are accelerated, it is possible that differences in ζ_2 among diffuse cloud sight lines can be attributed to the distance between a cloud and an acceleration site. Sight lines that probe material in close proximity to an acceleration site should show high ionization rates, while those that probe material farther away should show lower ionization rates. Unfortunately, defining acceleration sites and actually computing physical distances between those and the sample of observed clouds is difficult at best.

There are a few special cases, however, where the ionization rate can be inferred in molecular clouds known to be in close proximity to a site of cosmic-ray acceleration such as a supernova remnant. Shocked gas (e.g., Huang et al. 1986; Dickman et al. 1992) and OH (1720 MHz) masers (Claussen et al. 1997; Hewitt et al. 2006) observed toward the supernova remnant IC 443 demonstrate that the expanding shell is physically interacting with a foreground cloud, and gamma-ray observations of the remnant (Albert et al. 2007; Acciari et al. 2009; Abdo et al. 2010; Tavani et al. 2010) show a signature indicative of π^0 decay that suggests the cloud is experiencing a large flux of energetic protons. In Indriolo et al. (2010) we presented observations of H_3^+ in six sight lines that pass through molecular material near the supernova remnant IC 443. For the two sight lines where H_3^+ was detected, we inferred ionization rates of $\zeta_2 = 2.6^{+1.3}_{-1.9} \times 10^{-15}$ s^{-1} and $\zeta_2 = 1.6^{+0.8}_{-1.2} \times 10^{-15}$ s^{-1}—much higher than the mean value reported above—while in the remaining sight lines 3σ upper limits on ζ_2 were consistent with typical diffuse cloud values. Not only do these findings support the hypothesis that proximity to a site of particle acceleration controls the cosmic-ray ionization rate, but they also demonstrate variations in ζ_2 on length scales of a few pc.

8. SUMMARY

The survey of H_3^+ in diffuse molecular clouds now covers 50 sight lines, with detections in 21 of those. Cosmic-ray ionization rates (and upper limits) are inferred in all of these sight lines. Where H_3^+ is detected, ionization rates are in the range $(1.7 \pm 1.3) \times 10^{-16}$ s$^{-1} < \zeta_2 < (10.6 \pm 8.2) \times 10^{-16}$ s^{-1}. Accounting for upper limits, the mean value of the ionization rate is $\zeta_2 = (3.5^{+5.3}_{-3.0}) \times 10^{-16}$ s^{-1}. This is about one order of magnitude larger than ionization rates inferred from previous observations of other molecular species (e.g., OH and HD), although recent observations of OH$^+$ and H$_2$O$^+$ with *Herschel* are suggestive of high ionization rates as well (0.6×10^{-16} s$^{-1} < \zeta_H < 2.4 \times 10^{-16}$ s^{-1}; Neufeld et al. 2010). The lowest 3σ upper limits found for sight lines where H_3^+ is not detected are about $\zeta_2 < 0.4 \times 10^{-16}$ s^{-1}. Together, the wide range of inferred ionization rates and the low upper limits allude to variations in ζ_2 between different diffuse cloud sight lines.

Comparisons of ζ_2 with various line-of-sight properties (including Galactic latitude, Galactic longitude, and heliocentric distance) show no clear trends. This suggests that variations in the cosmic-ray ionization rate between different sight lines are caused not by large scale, but local effects. A comparison of ζ_2 with the total hydrogen column density (N_H) shows no strong correlation when only diffuse clouds are considered. When ionization rates inferred for dense cloud sight lines with much higher N_H are included though, ζ_2 is seen to decrease with increased N_H. This correlation is expected as low-energy cosmic rays—those most efficient at ionization—will lose all of their energy before reaching the interiors of dense clouds. The lack of a correlation amongst diffuse cloud sight lines suggests that the particles primarily responsible for ionization must be able to completely penetrate diffuse clouds, while the difference in ζ_2 between diffuse and dense clouds indicates that these same particles must be stopped in the outer layers of dense clouds.

Given that total column density—at least in the case of diffuse clouds—is unable to explain variations in the ionization rate, the concept of a cosmic-ray spectrum that is uniform throughout the Galaxy must be reconsidered. Instead, the flux of low-energy (MeV) cosmic rays is most likely controlled by proximity to local sites of particle acceleration. Our recent observations showing a high ionization rate toward the supernova remnant IC 443 (Indriolo et al. 2010) support this conjecture.

REFERENCES

Abdo, A. A., Ackermann, M., Ajello, M., et al. 2010, ApJ, 712, 459
Acciari, V. A., Aliu, E., Arlen, T., et al. 2009, ApJ, 698, L133
Ackermann, M., Ajello, M., Allafort, A., et al. 2011, Science, 334, 1103
Albert, J., Aliu, E., Anderhub, H., et al. 2007, ApJ, 664, L87
Black, J. H., & Dalgarno, A. 1977, ApJS, 34, 405
Black, J. H., Hartquist, T. W., & Dalgarno, A. 1978, ApJ, 224, 448
Bohlin, R. C., Savage, B. D., & Drake, J. F. 1978, ApJ, 224, 132
Brittain, S. D., Simon, T., Kulesa, C., & Rettig, T. W. 2004, ApJ, 606, 911
Cardelli, J. A., Meyer, D. M., Jura, M., & Savage, B. D. 1996, ApJ, 467, 334
Cartledge, S. I. B., Lauroesch, J. T., Meyer, D. M., & Sofia, U. J. 2004, ApJ, 613, 1037
Chevalier, C., & Ilovaisky, S. A. 1998, A&A, 330, 201
Claussen, M. J., Frail, D. A., Goss, W. M., & Gaume, R. A. 1997, ApJ, 489, 143
Conti, P. S., & Vacca, W. D. 1990, AJ, 100, 431
Crabtree, K. N., Indriolo, N., Kreckel, H., Tom, B. A., & McCall, B. J. 2011, ApJ, 729, 15
Cravens, T. E., & Dalgarno, A. 1978, ApJ, 219, 750
Dalgarno, A. 2006, Proc. Natl Acad. Sci., 103, 12269
de Zeeuw, P. T., Hoogerwerf, R., de Bruijne, J. H. J., Brown, A. G. A., & Blaauw, A. 1999, AJ, 117, 354
Dickman, R. L., Snell, R. L., Ziurys, L. M., & Huang, Y. 1992, ApJ, 400, 203
Federman, S. R., Weber, J., & Lambert, D. L. 1996, ApJ, 463, 181
Fruscione, A., Hawkins, I., Jelinsky, P., & Wiercigroch, A. 1994, ApJS, 94, 127
Geballe, T. R., McCall, B. J., Hinkle, K. H., & Oka, T. 1999, ApJ, 510, 251
Geballe, T. R., & Oka, T. 1996, Nature, 384, 334
Geballe, T. R., & Oka, T. 2010, ApJ, 709, L70
Gerin, M., de Luca, M., Black, J., et al. 2010, A&A, 518, L110
Gibb, E. L., Brittain, S. D., Rettig, T. W., et al. 2010, ApJ, 715, 757
Goto, M., McCall, B. J., Geballe, T. R., et al. 2002, PASJ, 54, 951
Goto, M., Usuda, T., Geballe, T. R., et al. 2011, PASJ, 63, L13
Goto, M., Usuda, T., Nagata, T., et al. 2008, ApJ, 688, 306
Hartquist, T. W., Black, J. H., & Dalgarno, A. 1978a, MNRAS, 185, 643
Hartquist, T. W., Doyle, H. T., & Dalgarno, A. 1978b, A&A, 68, 65

Hayakawa, S., Nishimura, S., & Takayanagi, T. 1961, PASJ, 13, 184
Herbst, E., & Klemperer, W. 1973, ApJ, 185, 505
Hewitt, J. W., Yusef-Zadeh, F., Wardle, M., Roberts, D. A., & Kassim, N. E. 2006, ApJ, 652, 1288
Hezareh, T., Houde, M., McCoey, C., Vastel, C., & Peng, R. 2008, ApJ, 684, 1221
Hinkle, K. H., Blum, R. D., Joyce, R. R., et al. 2003, Proc. SPIE, 4834, 353
Huang, Y., Dickman, R. L., & Snell, R. L. 1986, ApJ, 302, L63
Indriolo, N. 2011, PhD thesis, Univ. Illinois
Indriolo, N., Blake, G. A., Goto, M., et al. 2010, ApJ, 724, 1357
Indriolo, N., Geballe, T. R., Oka, T., & McCall, B. J. 2007, ApJ, 671, 1736
Jenkins, E. B., Jura, M., & Loewenstein, M. 1983, ApJ, 270, 88
Jensen, A. G., Rachford, B. L., & Snow, T. P. 2005, ApJ, 619, 891
Jura, M. 1975, ApJ, 197, 581
Karpas, Z., Anicich, V., & Huntress, W. T. 1979, J. Chem. Phys., 70, 2877
Käufl, H., Ballester, P., Biereichel, P., et al. 2004, Proc. SPIE, 5492, 1218
Klippenstein, S. J., Georgievskii, Y., & McCall, B. J. 2010, J. Phys. Chem. A, 114, 278
Kreckel, H., Motsch, M., Mikosch, J., et al. 2005, Phys. Rev. Lett., 95, 263201
Kreckel, H., Novotný, O., Crabtree, K. N., et al. 2010, Phys. Rev. A, 82, 042715
Kulesa, C. A. 2002, PhD thesis, Univ. Arizona
Lodders, K. 2003, ApJ, 591, 1220
Maíz-Apellániz, J., Walborn, N. R., Galué, H. Á., & Wei, L. H. 2004, ApJS, 151, 103
McCall, B. J. 2001, PhD thesis, Univ. Chicago
McCall, B. J., Drosback, M. M., Thorburn, J. A., et al. 2010, ApJ, 708, 1628
McCall, B. J., Geballe, T. R., Hinkle, K. H., & Oka, T. 1998, Science, 279, 1910
McCall, B. J., Geballe, T. R., Hinkle, K. H., & Oka, T. 1999, ApJ, 522, 338
McCall, B. J., Hinkle, K. H., Geballe, T. R., et al. 2002, ApJ, 567, 391
McCall, B. J., Huneycutt, A. J., Saykally, R. J., et al. 2003, Nature, 422, 500
McCall, B. J., Huneycutt, A. J., Saykally, R. J., et al. 2004, Phys. Rev. A, 70, 052716
McLean, I. S., Becklin, E. E., Bendiksen, O., et al. 1998, Proc. SPIE, 3354, 566
Mitchell, J. B. A. 1990, Phys. Rep., 186, 215
Mountain, C. M., Robertson, D. J., Lee, T. J., & Wade, R. 1990, Proc. SPIE, 1235, 25
Neufeld, D. A., Goicoechea, J. R., Sonnentrucker, P., et al. 2010, A&A, 521, L10
Nichols, J. S., & Slavin, J. D. 2004, ApJ, 610, 285
Nota, A., Pasquali, A., Clampin, M., et al. 1996, ApJ, 473, 946
O'Donnell, E. J., & Watson, W. D. 1974, ApJ, 191, 89
Oka, T., Geballe, T. R., Goto, M., Usuda, T., & McCall, B. J. 2005, ApJ, 632, 882
Padovani, M., Galli, D., & Glassgold, A. E. 2009, A&A, 501, 619
Pasquali, A., Nota, A., Smith, L. J., et al. 2002, AJ, 124, 1625
Rachford, B. L., Snow, T. P., Destree, J. D., et al. 2009, ApJS, 180, 125
Rachford, B. L., Snow, T. P., Tumlinson, J., et al. 2002, ApJ, 577, 221
Rakshit, A. B. 1982, Int. J. Mass Spectrom. Ion Phys., 41, 185
Ritchey, A. M., Federman, S. R., & Lambert, D. L. 2011, ApJ, 728, 36
Roberts, L. C., Jr., Gies, D. R., Parks, J. R., et al. 2010, AJ, 140, 744
Savage, B. D., Bohlin, R. C., Drake, J. F., & Budich, W. 1977, ApJ, 216, 291
Sheffer, Y., Rogers, M., Federman, S. R., et al. 2008, ApJ, 687, 1075
Shuping, R. Y., Snow, T. P., Crutcher, R., & Lutz, B. L. 1999, ApJ, 520, 149
Snow, T. P., Destree, J. D., Burgh, E. B., et al. 2010, ApJ, 720, L190
Snow, T. P., & McCall, B. J. 2006, ARA&A, 44, 367
Sofia, U. J., Lauroesch, J. T., Meyer, D. M., & Cartledge, S. I. B. 2004, ApJ, 605, 272
Sonnentrucker, P., Welty, D. E., Thorburn, J. A., & York, D. G. 2007, ApJS, 168, 58
Spitzer, L., Jr., & Tomasko, M. G. 1968, ApJ, 152, 971
Tavani, M., Giuliani, A., Chen, A. W., et al. 2010, ApJ, 710, L151
Theard, L. P., & Huntress, W. T. 1974, J. Chem. Phys., 60, 2840
Thorburn, J. A., Hobbs, L. M., McCall, B. J., et al. 2003, ApJ, 584, 339
Torres-Dodgen, A. V., Carroll, M., & Tapia, M. 1991, MNRAS, 249, 1
Tuthill, P. G., Monnier, J. D., Lawrance, N., et al. 2008, ApJ, 675, 698
van der Tak, F. F. S., & van Dishoeck, E. F. 2000, A&A, 358, L79
van Dishoeck, E. F., & Black, J. H. 1986, ApJS, 62, 109
van Dishoeck, E. F., & Black, J. H. 1989, ApJ, 340, 273
van Leeuwen, F. 2007, A&A, 474, 653
Watson, W. D. 1973, ApJ, 183, L17
Webber, W. R. 1998, ApJ, 506, 329